

Feature-based Inversion of 2.5D Controlled Source Electromagnetic Data using Generative Priors

Hongyu Zhou, *Graduate Student Member, IEEE*, Haoran Sun, *Graduate Student Member, IEEE*, Rui Guo, *Member, IEEE*, Maokun Li, *Fellow, IEEE*, Fan Yang, *Fellow, IEEE*, Shenheng Xu, *Member, IEEE*,

Abstract—In this study, we investigate feature-based 2.5D controlled source marine electromagnetic (mCSEM) data inversion using generative priors. Two-and-a-half dimensional modeling using finite difference method (FDM) is adopted to compute the response of horizontal electric dipole (HED) excitation. Rather than using a neural network to approximate the entire inverse mapping in a black-box manner, we adopt a plug-and-play strategy in which a variational autoencoder (VAE) is used solely to learn prior information on conductivity distributions. During the inversion process, the conductivity model is iteratively updated using the Gauss–Newton method, while the model space is constrained by projections onto the learned VAE decoder. This framework preserves explicit control over data misfit and enables flexible adaptation to different survey configurations. Numerical and field experiments demonstrate that the proposed approach effectively incorporates prior information, improves reconstruction accuracy, and exhibits good generalization performance.

Index Terms—2.5D electromagnetic modeling, electromagnetic data inversion, controlled source electromagnetics, generative models, generative priors, machine learning, deep learning, constrained inversion, joint inversion

I. INTRODUCTION

Electromagnetic (EM) methods have been widely used in geophysical prospecting. Among them, the controlled source electromagnetic (CSEM) method has been successfully used to evaluate targets with significant resistivity contrasts, including ore deposits, water bodies, and hydrocarbon reservoirs, etc [1]–[20]. This method involves stimulating the low-frequency EM field by artificial sources, measuring the EM field at selected locations, and inverting and interpreting the measurements with data inversion algorithms.

Accurate CSEM modeling is essential for reliable data inversion and interpretation. Due to the lack of translational symmetry in the horizontal electric dipole (HED) source, the EM field in CSEM surveys cannot be accurately simulated in a purely 2D space. A direct solution is to perform full 3D modeling [2], [4], but this approach is computationally expensive and resource-intensive. Alternatively, if the geological structure is assumed to vary only in two dimensions and remains constant along one direction, 2.5D modeling provides

This work was funded by the National Key Research and Development Program of China (2023YFB3905003), National Natural Science Foundation of China (624B2085), and the Science and Technology Project of CNPC (grant no. 08-01-2024).

Hongyu Zhou, Haoran Sun, Maokun Li, Fan Yang and Shenheng Xu are with the Department of Electronic Engineering, Beijing National Research Center for Information Science and Technology (BNRist), Tsinghua University, Beijing 100084, China (e-mail: maokunli@tsinghua.edu.cn).

Rui Guo is with Faculty of Math and Computer Science, Weizmann Institute of Science, Rehovot, Israel.

an efficient compromise [3], [7], [11]. It enables accurate representation of the EM field while significantly reducing computational cost, making it suitable for practical inversion and interpretation tasks.

EM data inversion is inherently ill-posed and nonlinear, often leading to non-unique or unstable solutions. To mitigate this, prior knowledge is typically incorporated to constrain the inversion. A common strategy is to add regularization terms, such as the L_1 norm or Tikhonov regularization [21]–[23]. However, simple regularizations may struggle to capture more complex prior information. An alternative approach involves reparameterizing the model in a compact transformed space, which can be constructed using various techniques. For instance, model-based inversion uses horizons and polygons to define regions with assumed uniform properties. The unknowns include the physical parameters within each region and the coordinates of boundary control points [24]–[27], which are typically optimized using gradient-based methods. While this reduces the number of unknowns, it is often sensitive to the initial model and prone to local minima.

Another strategy involves reparameterizing the model with a linear combination of global basis functions, such as Fourier or wavelets. This method has been applied in EM inversion [28]–[31] and seismic tomography [32]–[35]. However, selecting appropriate basis functions is often heuristic and lacks the flexibility to encode task-specific prior knowledge. The basis functions can also be constructed with machine learning methods. In hydrogeologic ERT inversion, for example, complex model patterns are described using a training dataset, and singular value decomposition (SVD) is applied to learn representative image bases [36].

Deep learning provides a powerful framework to distill the accumulation of human experience and historical data into neural models and conduct effective inference on similar tasks [2], [35]. Generative modeling [37] allows for learning the underlying data distribution and generating new samples consistent with prior knowledge. Unlike supervised learning, generative models are typically trained solely in the model space, independent of physical simulations. As a result, paired data and model samples are not required for constructing the training set. In recent years, generative models have been explored for inversion tasks across various domains, including biomedical imaging [38], [39], electromagnetic inverse scattering [40], [41], image processing [42], [43], and geophysical applications [44], [45]. Among the commonly used generative models, variational autoencoders (VAEs) and generative adversarial networks (GANs) learn nonlinear mappings from

the original data space to a lower-dimensional latent space, providing a compact representation that serves as a generative prior in the inversion process [37].

The generative prior can be integrated into the inversion process by directly cascading the generative model with the physical forward operator in the objective function [40], [41], [45], [46]. In this framework, gradients are directly back-propagated from the objective function to the latent variables. However, the nonlinearity of the generative model can lead the optimization process trapped in local minima [47]. This challenge becomes even more pronounced when the physical forward operator is also nonlinear, further complicating the optimization landscape. To address this, in some gradient-based optimization with projections (e.g., projected gradient descent, PGD), the updated model is iteratively projected back onto the prior space, which can be defined by the range of a VAE decoder or GAN generator [39], [43], [47]–[49]. However, these methods are primarily designed for linear inverse problems. When the forward operator is nonlinear and the solution space is 2.5D or 3D, the computational cost of first-order methods may become prohibitive.

In this work, we develop a feature-based 2.5D marine CSEM inversion framework regularized by a generative prior. Unlike recent end-to-end or latent-space inversion approaches that use neural networks to directly infer subsurface models from data, the proposed method retains a physics-driven Gauss–Newton inversion scheme and introduces a variational autoencoder (VAE) solely to constrain the admissible conductivity model space. The VAE is trained to learn the prior distribution of conductivity models and is incorporated through a series of projection steps, in which intermediate Gauss–Newton updates are periodically projected onto the decoder output space. This procedure enforces feature-level geological consistency without altering the forward operator or the data misfit formulation. The resulting plug-and-play strategy decouples prior learning from physical inversion and differs fundamentally from conventional generative-prior regularization approaches. The main contributions of this work are threefold:

- 1) We propose a plug-and-play deep learning framework for 2.5D marine CSEM inversion, in which neural networks are used only to learn conductivity-domain prior information while the physics-based Gauss–Newton inversion scheme is fully preserved.
- 2) We construct a feature-level generative prior using a variational autoencoder trained on synthetic conductivity models to encode geological prior information without modifying the physical forward modeling.
- 3) We develop a projected Gauss–Newton inversion scheme for marine CSEM, where intermediate model updates are periodically projected onto the decoder space to integrate generative priors into a conventional Hessian-based inversion framework.

Numerical and field experiments demonstrate that the proposed method effectively incorporates *a priori* knowledge into the inversion, leading to improved reconstruction quality and robust performance across different survey configurations.

II. METHOD

A. 2.5D forward modeling and Jacobian computation

Starting from the frequency domain Maxwell's equations, and neglecting the magnetic source, and using the j -notation, we have

$$\nabla \times \bar{\mathbf{E}} = -j\omega\mu\bar{\mathbf{H}}, \quad (1a)$$

$$\nabla \times \bar{\mathbf{H}} = j\omega\epsilon'\bar{\mathbf{E}} + \bar{\mathbf{J}}, \quad (1b)$$

where $\bar{\mathbf{E}}$, $\bar{\mathbf{H}}$ and $\bar{\mathbf{J}}$ are respectively the electric field, magnetic field and electric source in the spatial domain. ω is the angular frequency, μ is the permeability, and $\epsilon' = \epsilon - j\frac{\sigma}{\omega}$ is the complex permittivity in which σ is the conductivity and ϵ is the real permittivity [50].

In a typical 2.5D survey, the EM field has to be modelled in the 3D space (e.g., the response of the dipole excitation), while the distribution of physical parameter is only variant in the 2D plane but invariant along the third dimension. Without loss of generality, we assume the model extends along the x direction, and the EM field in the yo plane is of interest. Solving 2.5D problem generally involves transforming the field and source with Fourier transform along the spatially invariant dimension (x -direction), that is,

$$\hat{\mathbf{F}}(k_x, y, z) = \int_{-\infty}^{+\infty} \bar{\mathbf{F}}(x, y, z) e^{-jk_x x} dx, \quad (2a)$$

$$\bar{\mathbf{F}}(x, y, z) = \frac{1}{2\pi} \int_{-\infty}^{+\infty} \hat{\mathbf{F}}(k_x, y, z) e^{jk_x k_x} dk_x, \quad (2b)$$

where $\hat{\mathbf{F}}$ denotes the field or source in the wave-number domain, and \mathbf{F} can be either \mathbf{E} , \mathbf{H} or \mathbf{J} . Rewriting (1a) and (1b) in the wave-number domain, and neglecting the z component of \mathbf{J} , we have

$$\frac{\partial \hat{E}_z}{\partial y} - \frac{\partial \hat{E}_y}{\partial z} = -j\omega\mu\hat{H}_x, \quad (3a)$$

$$\frac{\partial \hat{E}_x}{\partial z} - jk_x\hat{E}_z = -j\omega\mu\hat{H}_y, \quad (3b)$$

$$jk_x\hat{E}_y - \frac{\partial \hat{E}_x}{\partial y} = -j\omega\mu\hat{H}_z, \quad (3c)$$

$$\frac{\partial \hat{H}_z}{\partial y} - \frac{\partial \hat{H}_y}{\partial z} = (j\omega\epsilon + \sigma)\hat{E}_x + \hat{J}_x, \quad (3d)$$

$$\frac{\partial \hat{H}_x}{\partial z} - jk_x\hat{H}_z = (j\omega\epsilon + \sigma)\hat{E}_y + \hat{J}_y, \quad (3e)$$

$$jk_x\hat{H}_y - \frac{\partial \hat{H}_x}{\partial y} = (j\omega\epsilon + \sigma)\hat{E}_z. \quad (3f)$$

Further organizing (3a)–(3f), we have

$$\begin{aligned} & -\frac{\partial}{\partial y} \left(\frac{y_0}{k_e^2} \frac{\partial \hat{E}_x}{\partial y} \right) - \frac{\partial}{\partial z} \left(\frac{y_0}{k_e^2} \frac{\partial \hat{E}_x}{\partial z} \right) + jk_x \frac{\partial}{\partial y} \left(\frac{1}{k_e^2} \frac{\partial \hat{H}_x}{\partial z} \right) \\ & - jk_x \frac{\partial}{\partial z} \left(\frac{1}{k_e^2} \frac{\partial \hat{H}_x}{\partial y} \right) + y_0 \hat{E}_x = -\hat{J}_x + \frac{\partial}{\partial y} \left(\frac{jk_x}{k_e^2} \hat{J}_y \right), \end{aligned} \quad (4a)$$

$$\begin{aligned} & -\frac{\partial}{\partial y} \left(\frac{z_0}{k_e^2} \frac{\partial \hat{H}_x}{\partial y} \right) - \frac{\partial}{\partial z} \left(\frac{z_0}{k_e^2} \frac{\partial \hat{H}_x}{\partial z} \right) + jk_x \frac{\partial}{\partial z} \left(\frac{1}{k_e^2} \frac{\partial \hat{E}_x}{\partial y} \right) \\ & - jk_x \frac{\partial}{\partial y} \left(\frac{1}{k_e^2} \frac{\partial \hat{E}_x}{\partial z} \right) + z_0 \hat{H}_x = -\frac{\partial}{\partial z} \left(\frac{z_0}{k_e^2} \hat{J}_y \right), \end{aligned} \quad (4b)$$

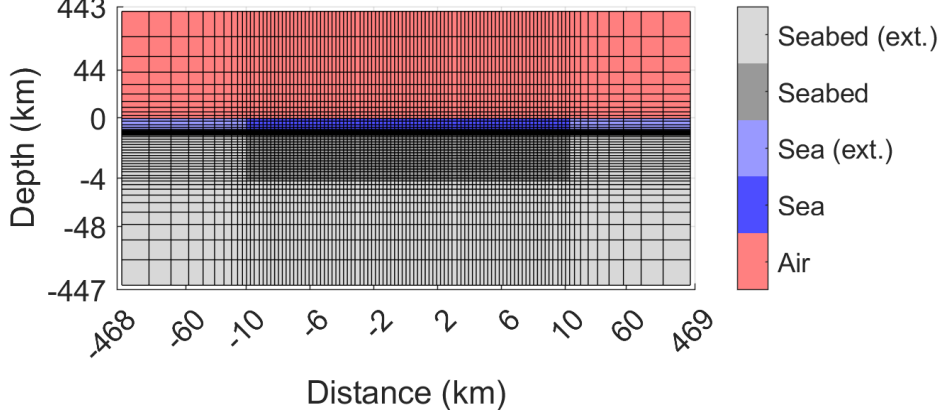


Fig. 1: Schematic of the finite difference mesh for 2.5D mCSEM forward modeling. "Ext." denotes the extended region.

where $k_e^2 = k_x^2 - k^2$, $k^2 = -z_0 y_0$, $z_0 = j\omega\mu$, $y_0 = j\omega\epsilon + \sigma$. Discretizing (4a) and (4b) with finite difference method (FDM), a set of linear equations can be derived and solved with respect to the x component electric and magnetic fields in the wave-number domain (\hat{E}_x and \hat{H}_x). Further resorting to (3a)-(3f), the y and z components of $\bar{\mathbf{E}}$ and $\bar{\mathbf{H}}$ can be computed, and the spatial domain fields $\bar{\mathbf{E}}$ and $\bar{\mathbf{H}}$ can be solved using the inverse Fourier transform in (2b). In this work, we focus on marine CSEM surveys, in which inline electric measurements (\bar{E}_y) are collected along the single survey line (extending along the y direction). Both transmitters and receivers are HEDs, whose orientations are along the survey line direction. We use the function $\mathcal{F}(\cdot)$ to represent the relationship between the conductivity σ and the measured \bar{E}_y at the receivers.

For the numerical simulation, the computational domain is discretized into square cells, and both the electric and magnetic fields in wave-number and spatial domains are defined at the center of each cell.

A schematic of the adopted FDM mesh is shown in Fig. 1. For clarity, the coordinates shown in the figure are not scaled to the actual physical distances, and the number of grid points is proportionally reduced to avoid an overly dense mesh illustration. Fig. 1 shows the entire computational domain, within which the seabed region of interest (i.e., domain of investigation, DoI) is indicated in dark gray. Above the DoI is the seawater layer, shown in dark blue, and the interface between the seawater and the DoI can be either flat or undulating. The mesh is refined near the seawater–DoI interface and gradually transitions to a coarser mesh away from the interface. Both the seawater layer and the DoI are extended in the horizontal direction. The DoI is also extended downward, and an air layer is located above the seawater. The extended region and the air layer are both discretized using nonuniform meshes, in which the grid spacing increases logarithmically away from the central region. Thirty cells are used in each direction, and the thickness of the outermost cells is set to 100 km. In Fig. 1, the extended cells and air cells are colored light blue, light gray, and red, respectively.

The Jacobian matrix can be computed with adjoint method [3], [51]. The relationship between the adjoint field, adjoint

source and the sensitivity can be formulated with [51]

$$\int_D (\bar{\mathbf{J}}_m^+ \cdot \frac{\partial \bar{\mathbf{H}}}{\partial \sigma_k} + \bar{\mathbf{J}}_e^+ \cdot \frac{\partial \bar{\mathbf{E}}}{\partial \sigma_k}) d\nu = \int_D \bar{\mathbf{E}}^+ \cdot \bar{\mathbf{E}} \phi_k d\nu, \quad (5)$$

where ϕ_k is the basis function at the k -th pixel, D is the effective domain of ϕ_k , and $\bar{\mathbf{J}}_m^+$, $\bar{\mathbf{J}}_e^+$ and $\bar{\mathbf{E}}^+$ are respectively adjoint magnetic source, electric source and electric field. The sensitivity of \bar{E}_y to conductivity σ can be written with

$$\frac{\partial \bar{E}_y}{\partial \sigma} = \int_{-\infty}^{+\infty} \int_D \bar{\mathbf{E}}_{J_y}^+ \cdot \bar{\mathbf{E}} ds dy. \quad (6)$$

where ds denotes the infinitesimal size inside effective domain D , dy denotes the infinitesimal length along the y direction, and $\bar{\mathbf{E}}_{J_y}^+$ is the adjoint electric field excited with y -direction electric source. (6) represents the integration of the product of the spatial electric fields within a rectangular prism with a base D and infinitely extending along y direction. Transforming both $\bar{\mathbf{E}}_{J_y}^+$ and $\bar{\mathbf{E}}$ to wave-number domain with (2a), (6) can be expressed with

$$\frac{\partial \bar{E}_y}{\partial \sigma} = \frac{1}{2\pi} \int_{-\infty}^{+\infty} \int_D \hat{\mathbf{E}}_{J_y}^+(-k_x, y, z) \cdot \hat{\mathbf{E}}(k_x, y, z) ds dk_x. \quad (7)$$

Noticing that \bar{E}_x is an odd function of k_x while \bar{E}_y and \bar{E}_z are even functions of k_x , (7) can finally be expressed with

$$\frac{\partial \bar{E}_y}{\partial \sigma} = \frac{1}{\pi} \int_0^{+\infty} \int_D (-\hat{E}_{J_y, x}^+ \hat{E}_x + \hat{E}_{J_y, y}^+ \hat{E}_y + \hat{E}_{J_y, z}^+ \hat{E}_z) ds dk_x. \quad (8)$$

B. Variational autoencoder (VAE)

The variational autoencoder (VAE) is a typical generative neural network structure, which is able to learn the distribution from the training dataset and generate new realizations conforming to the prior distribution [52], [53]. Generally, VAE is composed of an encoder \mathcal{E} and a decoder \mathcal{D} . In this framework, the encoder-decoder structure provides a probabilistic mapping between the high-dimensional conductivity model space and a compact latent space, enabling the extraction of representative geological features from training samples. The encoder input is the data sampled from the prior distribution, and the encoder

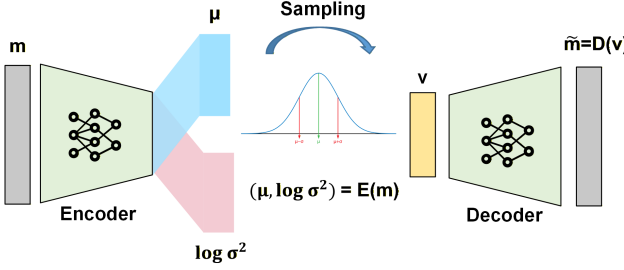


Fig. 2: Schematic of the variational autoencoder used in this work.

outputs respectively describe the mean and variance of a high-dimensional Gaussian distribution. This stochastic encoding allows different realizations sharing similar structural features to be represented by nearby latent variables, which is essential for enforcing feature-level consistency during inversion. Denoting the encoder input with \mathbf{m} , the output can be expressed with

$$\mathcal{E}(\mathbf{m}) = (\mathcal{E}_1(\mathbf{m}), \mathcal{E}_2(\mathbf{m})) = (\mu_{\mathcal{E}}, \log \sigma_{\mathcal{E}}^2), \quad (9)$$

where $\mu_{\mathcal{E}}$ and $\sigma_{\mathcal{E}}^2$ are respectively the mean and variance of a Gaussian distribution $\mathcal{N}(\mu_{\mathcal{E}}, \sigma_{\mathcal{E}}^2)$, from which the latent variable \mathbf{v} is sampled:

$$\mathbf{v} \sim \mathcal{N}(\mu_{\mathcal{E}}, \sigma_{\mathcal{E}}^2). \quad (10)$$

\mathbf{v} is then input into the decoder \mathcal{D} , yielding the reconstruction of \mathbf{m} :

$$\tilde{\mathbf{m}} = \mathcal{D}(\mathbf{v}). \quad (11)$$

The training objectives of the VAE are two-fold: making the reconstruction loss of VAE as small as possible, and simultaneously make the latent space approximate a standard normal distribution as close as possible. After training, the decoder defines an implicit model manifold, onto which intermediate inversion results can be projected to constrain the solution space without altering the physical forward operator. The objective function in VAE training can be expressed with

$$\mathcal{L} = \mathcal{L}_{\text{rec}} + \lambda \sum_{q=1}^Q (\mu_{\mathcal{E},q}^2 + \sigma_{\mathcal{E},q}^2 - \log \sigma_{\mathcal{E},q}^2 - 1). \quad (12)$$

Here, \mathcal{L}_{rec} is the reconstruction loss, Q is the dimension of the latent space, and λ is the coefficient adjusting the relative weight of the reconstruction loss and Kullback-Leibler divergence loss. For a more detailed derivation of the objective function please refer to [52]. After the training is finished, the decoder \mathcal{D} can be regarded as a data generator that characterizes the prior distribution and is able to generate new realizations conforming to the prior distribution.

The specific implementation of the VAE is not unique. In our implementation, the VAE is fine-tuned from the k1 – 8f VAE introduced in the noted latent diffusion work [54]. A schematic showing the structure is illustrated in Fig. 2, and the detailed structure of the VAE is included in Fig. S1 of the Supplementary Materials. The VAE have 86 million trainable parameters and 17 million non-trainable parameters in total.

The three channel input and output are respectively merged into one channel by averaging parameter values along the channel direction. In our implementation, the reconstruction loss \mathcal{L}_{rec} as included in (12) is composed of the L_2 loss both in the pixel domain and feature domain, i.e.,

$$\mathcal{L}_{\text{rec}} = \|\mathbf{m} - \tilde{\mathbf{m}}\|_2^2 + \gamma \|\mathcal{G}(\mathbf{m}) - \mathcal{G}(\tilde{\mathbf{m}})\|_2^2, \quad (13)$$

where $\mathcal{G}(\cdot)$ denotes a pre-trained and frozen image processing neural network such as AlexNet [55], and γ is the hyper-parameter adjusting the relative weights of the two types of loss. The inclusion of the feature domain loss aims to better capture the detailed features of small-sized layers.

C. Feature-based 2.5D CSEM inversion

In the deterministic EM inversion framework, the 2.5D CSEM inversion can be formulated as optimizing the unknown model \mathbf{m} by minimizing a loss function composed of both the data misfit term and the Tikhonov regularization [56], i.e.,

$$\mathcal{L}(\mathbf{m}) = \|\mathbf{W}_d(\mathbf{d}_{\text{obs}} - \mathcal{F}(\mathbf{m}))\|^2 + \alpha \|\mathbf{W}_m \mathbf{m}\|^2, \quad (14)$$

and

$$\hat{\mathbf{m}} = \arg \min_{\mathbf{m} \in \mathcal{S}} \mathcal{L}(\mathbf{m}). \quad (15)$$

Here, \mathbf{m} is the 2D conductivity distribution in the seabed, \mathbf{d}_{obs} is the measured complex value y component electric field as introduced in Section II-A, and $\mathcal{S} \subseteq \mathbb{R}^{N_m}$ is a set that captures the distribution that \mathbf{m} is *a priori* required to obey (e.g., non-negativity). In this work, we adopt a more informative generative prior described by the range of VAE decoder ($\mathcal{R}(\mathcal{D})$), i.e.,

$$\hat{\mathbf{m}} = \arg \min_{\mathbf{m} \in \mathcal{R}(\mathcal{D})} \mathcal{L}(\mathbf{m}). \quad (16)$$

As suggested by existing works [40], [41], [45], [46], one possible approach to solve (16) is to reformulate the optimization problem in the latent space \mathbb{R}^Q , i.e.,

$$\hat{\mathbf{v}} = \arg \min_{\mathbf{v} \in \mathbb{R}^Q} \|\mathbf{W}_d(\mathbf{d}_{\text{obs}} - \mathcal{F}(\mathcal{D}(\mathbf{v})))\|^2 + \alpha \|\mathbf{W}_m \mathcal{D}(\mathbf{v})\|^2, \quad (17)$$

and obtain the optimized model $\hat{\mathbf{m}}$ from the optimized latent variable $\hat{\mathbf{v}}$, i.e.,

$$\hat{\mathbf{m}} = \mathcal{D}(\hat{\mathbf{v}}). \quad (18)$$

However, we find (from both reports in [47], [48] and our numerical experiments) that (17) can be easily stuck in local minima, since the cascade of two nonlinear operators \mathcal{F} and \mathcal{D} exaggerates the ill-posedness of the problem. References [47], [48] solve (16) with projected gradient-descent (PGD), that is, in each iteration \mathbf{m} is first updated with gradient descent method and then projected to the $\mathcal{R}(\mathcal{D})$ set. However, first-order optimizations can take hundreds or even thousands of iterations to converge. Since in a 2.5D EM survey, each forward modeling and gradient computation requires solving dozens of linear systems with tens of thousands of unknowns, higher-order optimizations (e.g., Gauss-Newton) are preferred to accelerate the convergence.

We solve (17) with a projected Gauss-Newton (PGN) method [57], [58]. Similar to PGD, the PGN can also be

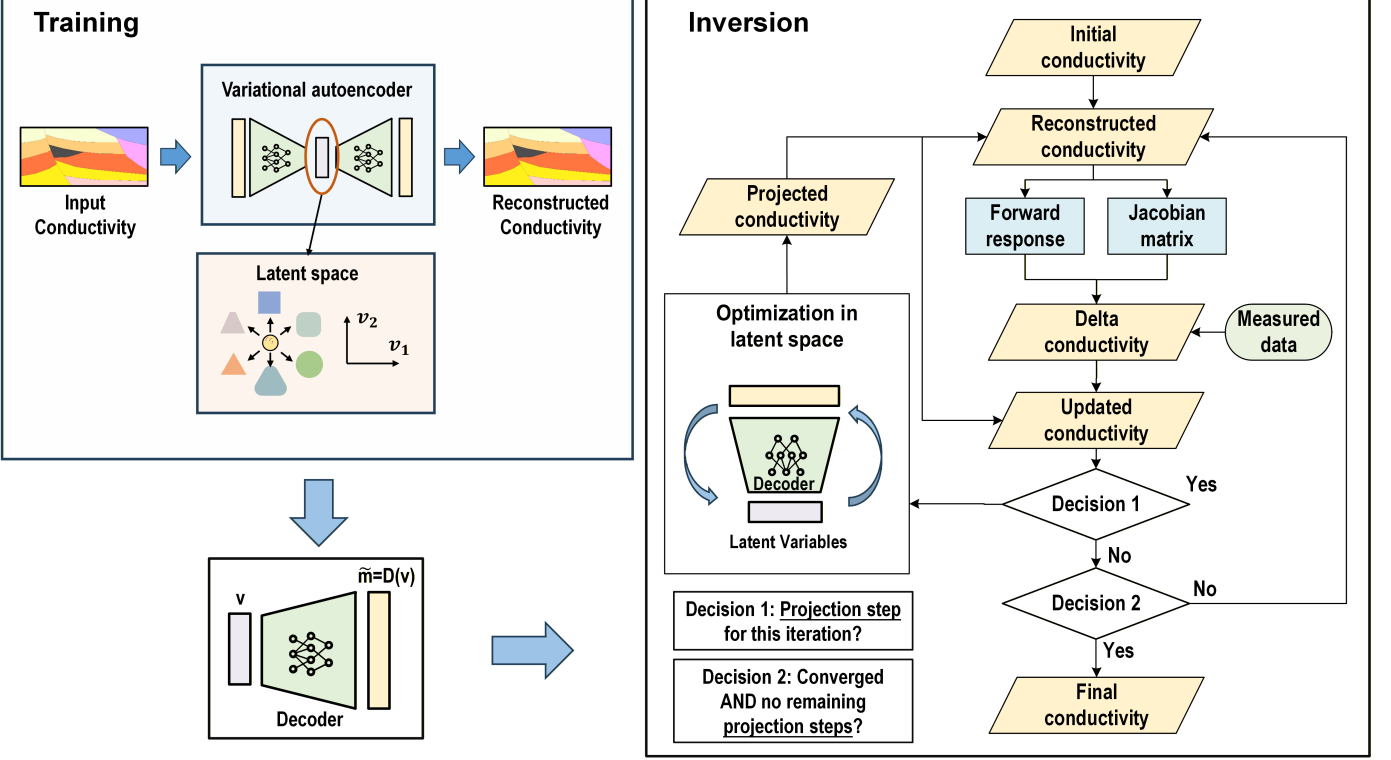


Fig. 3: The workflow of the proposed method consists of two stages: training and inversion. In the training stage, a variational autoencoder (VAE) is used to learn prior patterns in conductivity models. After training, the decoder is extracted and incorporated into the inversion stage, where iteratively updated conductivity models are projected onto the output space of the decoder. This approach differs from supervised end-to-end schemes, which typically require paired (data, model) examples for training.

separated into two stages. At the k -th iteration, \mathbf{m} is first updated with Gauss-Newton method, that is

$$\mathbf{m}_{k+1} = \mathbf{m}_k - \mathbf{H}_k^{-1} \mathbf{g}_k, \quad (19)$$

where \mathbf{H}_k and \mathbf{g}_k are respectively Hessian matrix and gradient of $\mathcal{L}(\mathbf{m})$ with respect to \mathbf{m} at the k -th iteration:

$$\mathbf{H}_k = \mathbf{J}_k^T \mathbf{W}_d^T \mathbf{W}_d \mathbf{J}_k + \alpha \mathbf{W}_m^T \mathbf{W}_m, \quad (20a)$$

$$\mathbf{g}_k = -\mathbf{J}_k^T \mathbf{W}_d^T \mathbf{W}_d (\mathbf{d}_{\text{obs}} - \mathcal{F}(\mathbf{m}_k)) + \alpha \mathbf{W}_m^T \mathbf{W}_m \mathbf{m}_k, \quad (20b)$$

where \mathbf{J}_k is the Jacobian matrix calculated by (5)-(8). In the second stage, the updated \mathbf{m}_k is projected to $\mathcal{R}(\mathcal{D})$ by solving the following minimization problem:

$$\hat{\mathbf{v}}_{k+1} = \arg \min_{\mathbf{v}} \|\mathbf{m}_{k+1} - \mathcal{D}(\mathbf{v})\|_2^2, \quad (21)$$

and compute the $\hat{\mathbf{m}}_{k+1}$ with (18). The inversion terminates when the data misfit reaches a predefined level or exceeds the maximum iterations. The workflow of the proposed inversion is shown in Fig. 3. We would like to point out that in the inversion, the projection is only conducted at several *projection steps* (the total number is generally smaller than 5 and with intervals between each other) instead of each iteration. The aim is to minimize the generalization risk of VAE therefore reducing the possibility that the inversion is trapped in the local minima. In addition, because the total number of projections is relatively small, and the time to solve (21) is not a computational bottleneck compared to the time for

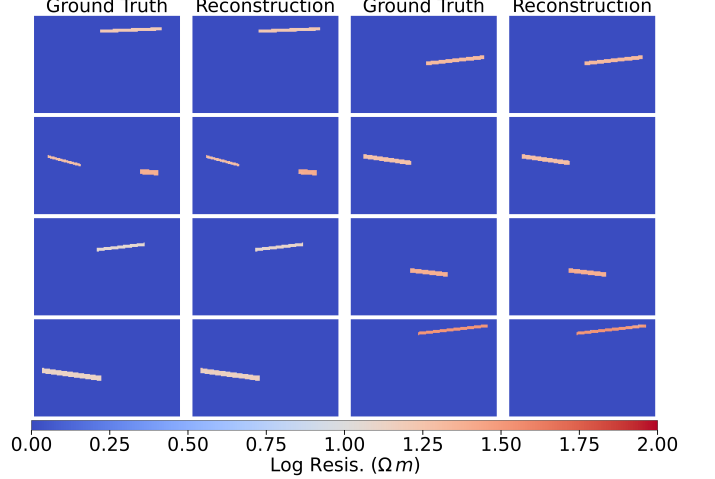


Fig. 4: Visualization of some example images in the training dataset and corresponding reconstructions.

forward modeling and gradient computation, we directly use first-order gradient descent (e.g., adaptive moment estimation (ADAM, [59])).

III. NUMERICAL EXPERIMENTS

A. VAE Algorithm Test

A fine-tune dataset containing 50000 images is simulated, 90% used for training and 10% for validation. Each image has

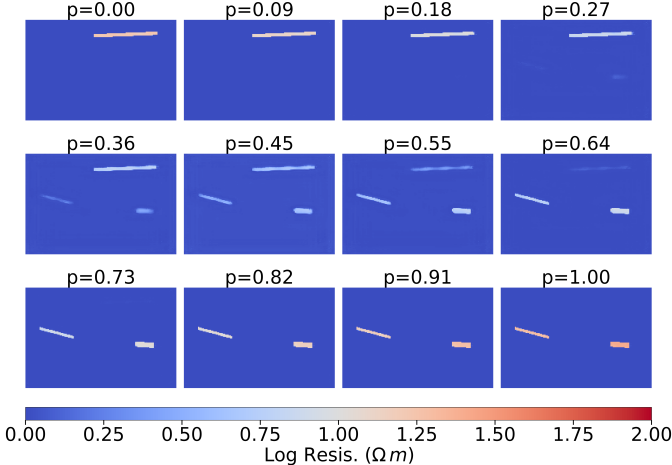


Fig. 5: Visualization of intermediate models transferring between two ground truth models in Fig. 4.

a size of 128×128 , and has a pattern of one or two thin resistive layers exist in the uniform conductive background. This corresponds to the *a priori* knowledge that, the DoI contains a thin and layer-shaped resistive hydrocarbon reservoir residing in the uniform conductive seabed, but the location, shape and size of the layer is to be determined in the inversion. The attribute value is set to 0 for the background and sampled from uniform distribution $\mathcal{U}(1.3, 2)$ for the layers. Some examples in the training dataset is shown in Fig. 4. The fine-tuning converges in 10 steps.

After the training finished, the performance of the fine-tuned VAE is tested. First, the ground truth models \mathbf{m} are compared to the corresponding VAE reconstructions $\mathbf{m}_{\text{rec}} = \mathcal{D}(\mathcal{E}_1(\mathbf{m}))$. Second, the continuity of the latent space is checked: given two models \mathbf{m}_1 and \mathbf{m}_2 and their corresponding latent variables $\mathbf{v}_1 = \mathcal{E}_1(\mathbf{m}_1)$ and $\mathbf{v}_2 = \mathcal{E}_1(\mathbf{m}_2)$, the intermediate models $\mathbf{m}_{1,2,p} = \mathcal{D}((1-p)\mathbf{v}_1 + p\mathbf{v}_2)$ are calculated. As shown in Figs. 4 and 5, the reconstructions well resemble the ground truths, and the reconstructed models can transform smoothly between each other. The two experiments together verify the efficacy of the VAE.

B. Simple Model Test

We set up the same survey configuration as adopted in [3] to verify the correctness of the proposed algorithm. The DoI ranges from 0 to 20 km horizontally and from -4 to -1 km vertically, with a 1-km-thick seawater layer above it. Forty-one inline electric dipoles are uniformly distributed at the depth of 950 m, excited one at a time, and twenty-one receivers are uniformly distributed on the seafloor. We adopt a nonuniform mesh that is refined in the transmitter-receiver region and uniform elsewhere, with 251 grids in the horizontal direction and 156 grids in the vertical direction. Fig. 6 shows the survey geometry and transmitter-receiver configuration introduced in this section. The transmitters are denoted by red circles, and the receivers are denoted by black crosses.

Based on the survey geometry and transceiver configurations shown in Fig. 6, we generate three ground truth models,

respectively referred to as test model A, B and C, to simulate marine hydrocarbon exploration scenarios involving thin resistive layers with different shapes and geometries embedded in the seabed. Test model A is shown in both Fig. 6 and Fig. 7a, and test model B and C are respectively shown in Figs. 7b and 7c. Test models A and B contain resistive layers 1 km below the seabed, and the resistivities of the seawater, sedimentary background and resistive layers are respectively $0.33 \Omega\text{m}$, $1 \Omega\text{m}$ and $20 \Omega\text{m}$. In test model A, the 8-km-length resistive layer is tilted by 2 degrees, while in test model B, three shorter resistive layers with lengths of 2.5 km, 3 km, and 2.5 km are arranged in parallel and separated by two 1.5-km gaps. Test model C contains two 4-km-long resistive layers, one is 120 m thick, located 800 m below the seafloor and has a resistivity of $20 \Omega\text{m}$, while the other is 240 m thick, located 1500 m below the sea floor and has a resistivity of $100 \Omega\text{m}$. The background sedimentary layer has a resistivity of $1.43 \Omega\text{m}$. In this experiment, the adopted frequencies are 0.25 and 0.75 Hz. Five-percent Gaussian noise is added to the simulated data in each case using (22):

$$d_{\text{obs},mnk}^{\text{noise}} = d_{\text{obs},mnk}(1 + \beta(n_{1,mnk} + in_{2,mnk})), \quad (22)$$

where β is the noise level, and $n_{1,mnk}$ and $n_{2,mnk}$ are independently sampled from standard normal distribution $\mathcal{N}(0, 1)$. m , n and k are respectively the index of transmitter, receiver and frequency.

We conducted inversions with conventional L_2 regularization, weighted L_2 regularization and the proposed feature-based inversion (abbreviated as L_2 , WL_2 and FB hereafter). For the three test models, the initial models are uniform backgrounds of $1 \Omega\text{m}$, $1 \Omega\text{m}$ and $1.43 \Omega\text{m}$, which are identical for all inversions. The reconstructed models obtained by L_2 , WL_2 and FB inversion are respectively shown in the second, third and fourth rows of Fig. 7. For a clearer comparison, in each model we select two depth traces (Line1 and Line2, whose locations are shown by black dash lines in Figs. 7a, 7b and 7c). The resistivity distributions of the ground truth models and reconstructions along the traces are presented in Figs. 8a to 8f, and data misfit curves are displayed in Figs. 8g to 8i.

In both L_2 and WL_2 reconstructions, the resistive layers in all three test models can be identified with distinguishable boundaries, and their locations and sizes show no large deviations from the ground truth. However, in the conventional inversions, the recovered layers are shallower than their actual depths, with deviations of about 300–400 m, and the layer thickness is overestimated. For example, in WL_2 reconstruction the resistive layer is about twice the real thickness. In WL_2 reconstructions, conductive anomalies can be observed across the three cases. For example, in Fig. 7g, one of the conductive anomalies is close to the upper surface of the resistive layer, and the other is below the resistive layer with offset ranging from 8 to 12 km and depth at about 3 km. We note that similar artifact patterns in 2.5D mCSEM inversion have also been reported in previous studies (for instance, see Figure 7 in [3]), which reflect the non-uniqueness of the solution and hinder accurate reservoir evaluation.

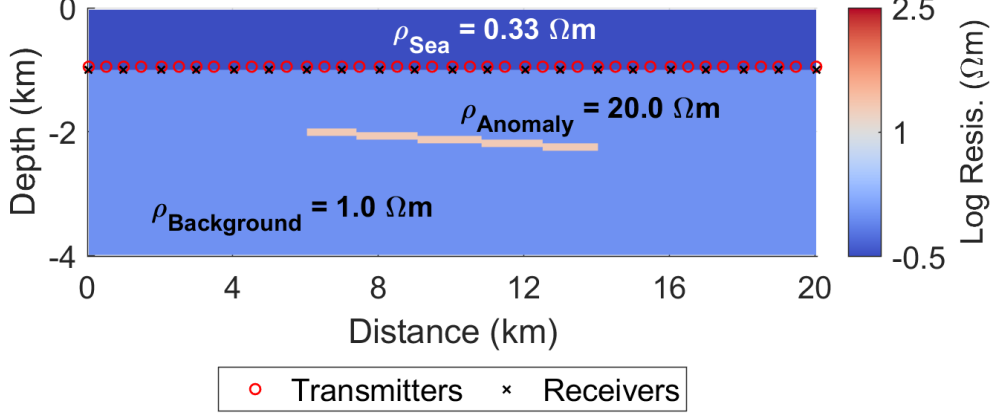


Fig. 6: A visualization of test model A. Forty-one transmitters and twenty-one receivers are respectively positioned at the depth of 950 m and 1000 m. The resistivities of the seawater, seabed background, and resistive anomaly are clearly labeled in the image.

Comparing the inversion results, clear improvements in FB inversions can be observed. Across Figs. 8a to 8f, the resistivity curves reconstructed by FB (plotted in red) are closer to the ground truth curves (plotted in black) than those obtained by L_2 (plotted in blue) and WL_2 (plotted in green). The artifacts observed in conventional inversions are largely suppressed, yielding more uniform backgrounds and well-resolved targets whose depths, thicknesses, and attribute values closely match the corresponding ground truth models. Across the three test models, both L_2 and FB inversions converge within 10–15 iterations with final data misfits close to the noise level, while the WL_2 inversion appears to be trapped in local minima for test models A and C. In the feature-based inversions, the *projection steps* are iterations 2, 4, 6 and 8 for test model A and B, and at iterations 2, 4, 6, 8 and 10 for test model C. The pairs of points with the same horizontal coordinates on the FB data misfit convergence curves in Figs. 8g–8i respectively represent the data misfits before and after these projections.

We also highlight the generalization ability of the proposed method: resistive layers with different shapes, such as inclined layers or layers composed of discontinuous segments, can be clearly delineated. We attribute this to the fact that the adopted VAE achieves a balance between reconstruction accuracy and generalization. Pre-training on a diverse set of natural images allows the neural network to learn general and rich prior knowledge for image feature extraction and reconstruction. In the fine-tuning stage, this prior knowledge is efficiently transferred to the distribution space of the conductivity model to be reconstructed.

Some metrics, including data misfit (DM), intersection over union (IoU), mean square error (MSE) and structural similarity (SSIM), are adopted to assess the reconstructions. Their definitions are introduced in Appendix, and the results of test models A–C are reported in Table I. L_2 reconstructions presents better MSE than WL_2 , which may be explained by the observation that WL_2 inversion tends to introduce conductive anomaly with larger conductivities and thicker resistive layers

compared to L_2 inversion. In contrast, WL_2 reconstructions outperform L_2 in SSIM, which may be explained by the observation that WL_2 yields a clearer boundary and more unique background compared to L_2 inversion. Both L_2 and WL_2 inversions have their own features, however, in all the experiments, the FB reconstructions outperform them in all the three model domain metrics.

To find out how the reconstruction is updated in the feature-based inversion, we visualize the evolution of test model C in FB inversion in Fig. 9. The models updated with Gauss–Newton optimization in the i -th iteration are indexed *Ite- i* , and the projections of *Ite- i* models to $\mathcal{R}(\mathcal{D})$ are indexed *Ite- i -Projected*. Comparing models before and after the projection, the non-uniform background and conductive anomalies are effectively suppressed and become more uniform, thereby alleviating non-uniqueness and avoiding convergence to local minima.

TABLE I: The comparison of data misfit (DM), intersection over union (IoU), mean square error (MSE) and structural similarity (SSIM) of test models A–C.

	Methods	DM	IoU	MSE	SSIM
Test model A	L_2	0.227%	0.021	0.0234	0.619
	WL_2	0.551%	0	0.0432	0.628
	FB	0.230%	0.500	0.0079	0.907
Test model B	L_2	0.224%	0.146	0.0140	0.642
	WL_2	0.267%	0.200	0.0168	0.704
	FB	0.311%	0.675	0.0045	0.933
Test model C	L_2	0.222%	0.341	0.0191	0.840
	WL_2	0.372%	0.196	0.0523	0.853
	FB	0.269%	0.416	0.0110	0.957

C. Simple Model Test with Noise

In this section, we investigate the impact of the noise level on the feature-based inversion. Test model C is adopted here, and the configurations of the DoI, mesh, operating frequency, transmitters and receivers are the same as those in Section III-B, while the noise level is changed to 15%, 25% and 50%,

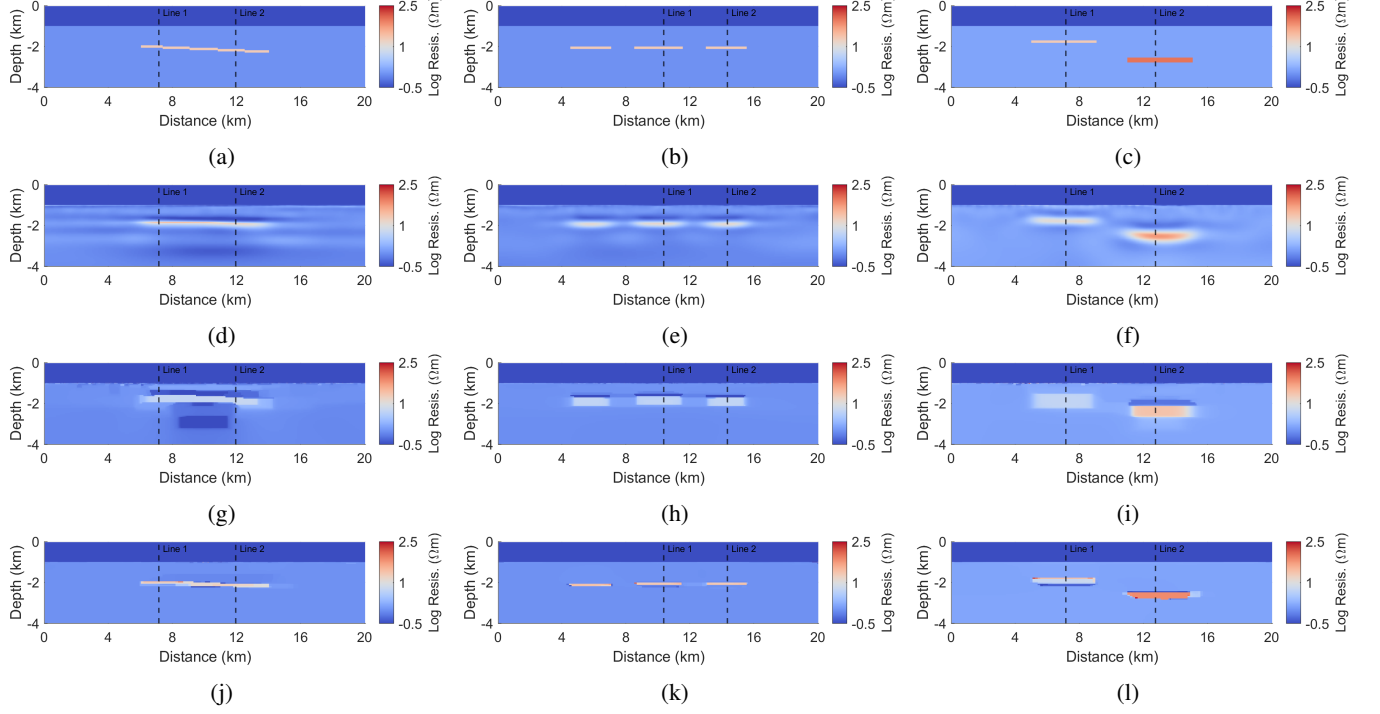


Fig. 7: The ground truth models and reconstructed models as introduced in Section III-C. The four rows from top to bottom respectively represent the ground truth models, reconstructed models with L_2 regularization, WL_2 regularization and feature-based inversion.

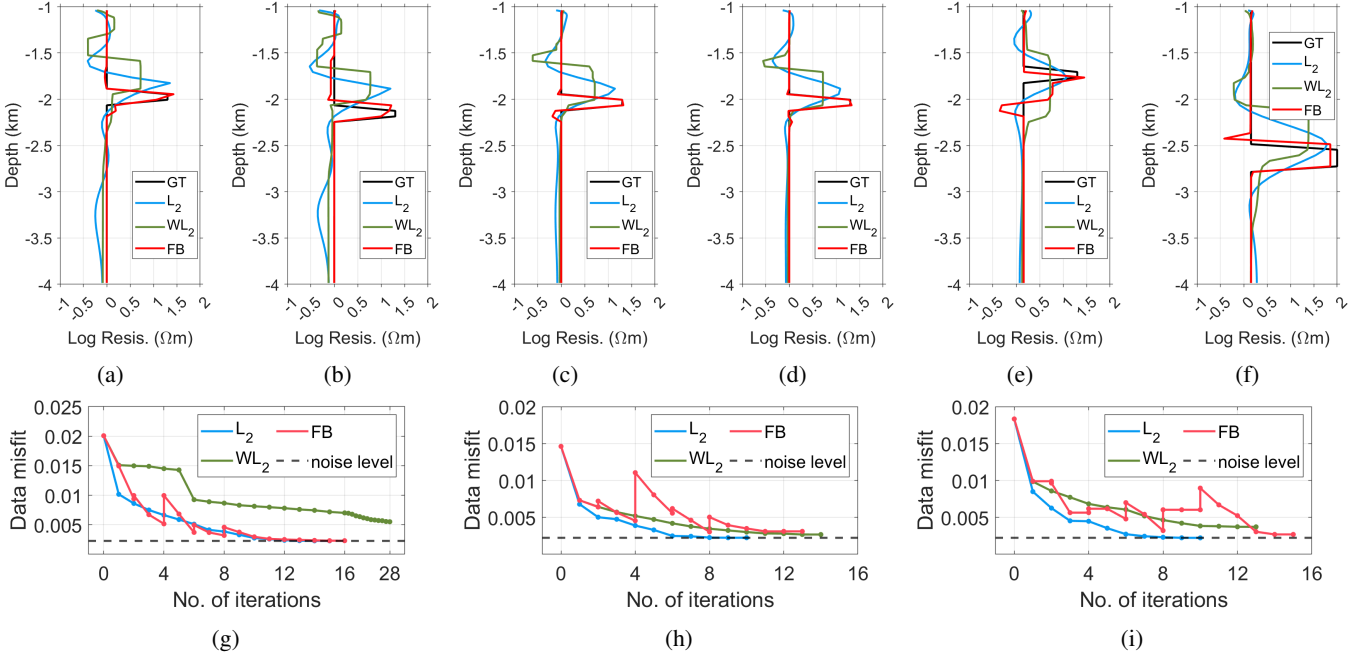


Fig. 8: Figs. 8a and 8b respectively show the ground truth and recovered resistivity curves at Line1 and Line2 (the locations are denoted with black dash lines in Fig. 7a), and Fig. 8g display the data misfit during the reconstruction of test model A. Similarly, Figs. 8c, 8d and 8h show the resistivity curves corresponding to Line1 and Line2 in Fig. 7b, and data misfit corresponding to test model B. Figs. 8e, 8f and 8i show the resistivity curves corresponding to Line1 and Line2 in Fig. 7c, and data misfit corresponding to test model C.

respectively. Fig. 10 shows a comparison between noise-free simulated data and data with different noise levels, excited

by transmitters located at 2.52 km, 7.48 km, 12.52 km, and 17.48 km, corresponding to test model C. The DMs introduced

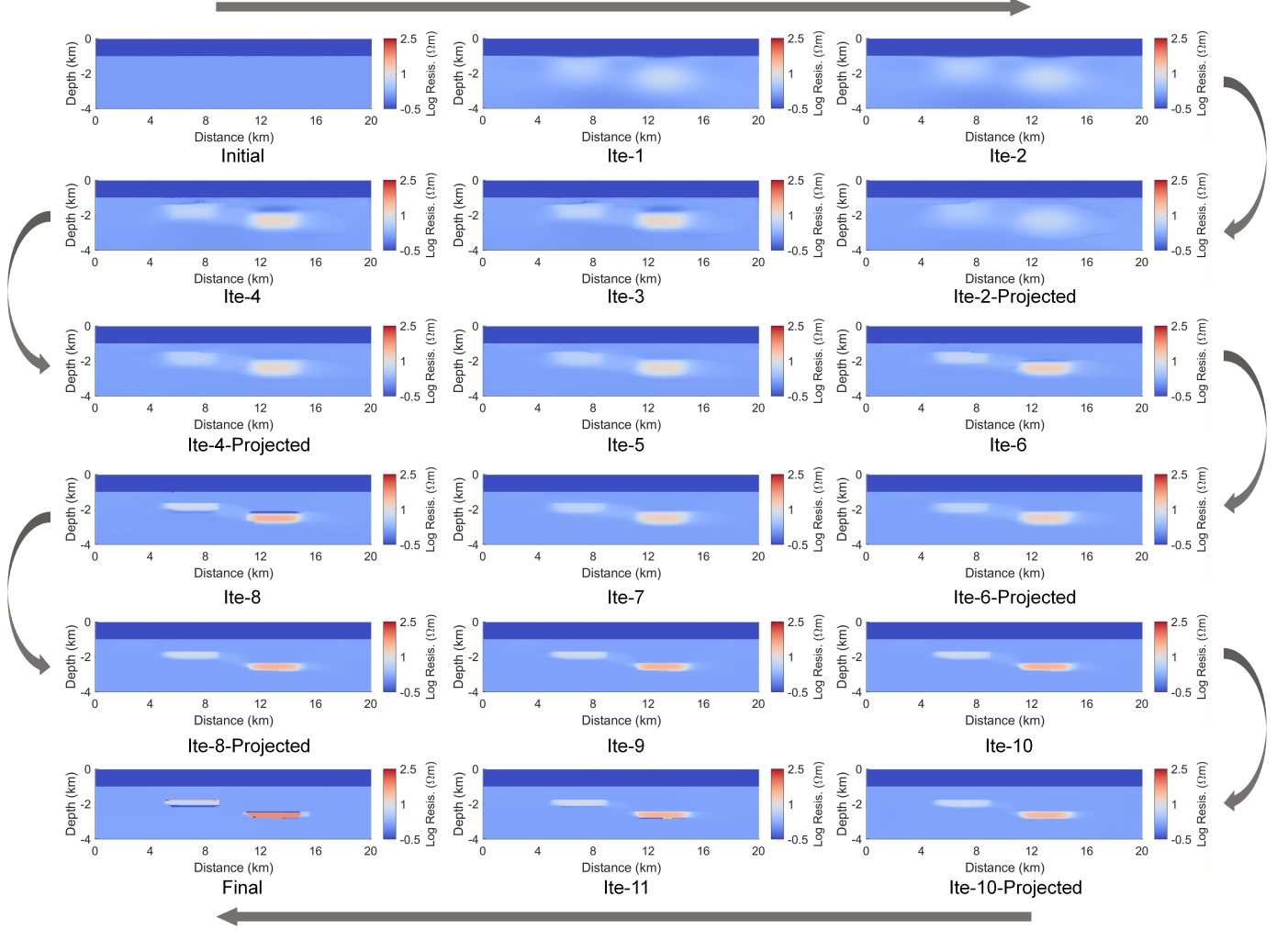


Fig. 9: The model evolution in the feature-based inversion of test model C as reported in Section. III-B.

by 15%, 25% and 50% noise are respectively 0.0071, 0.0127 and 0.0322 (also calculated using (A1)). L_2 , WL_2 and FB reconstructions using different levels of noise are shown in Fig. 11. The reconstructed resistivity traces as well as the data misfit curves are displayed in Fig. 12.

With the noise increasing from 5% to 50%, all the three inversions converge to the corresponding noise levels; however, the reconstruction quality degrades in all cases, which is expected. Reconstruction patterns similar to those reported in Section. III-B are observed again: blurred resistivity layer boundaries for L_2 inversions, overestimated thickness and conductive anomalies above the resistive layer in WL_2 inversions, and the less uniform background for all the inversions. However, across all noise levels, the FB reconstructions consistently perform the best among the three methods, with resistive layers more clearly delineated. Even under the noise level of 50%, the geometries of the resistive layers remain identifiable. This may benefit reservoir interpretation when the measured data quality is limited.

A clearer observation of the above findings can be obtained by comparing the ground truth and reconstructed resistive depth traces in Figs. 12a–12f. Although resistive anomalies can be captured, two major problems are observed in L_2

and WL_2 inversions: a vertical shift from the true depth of the resistive layer and an accompanying thin conductive layer above the resistive layer (both phenomena are more pronounced for the right layer, likely due to its greater burial depth and higher resistivity contrast than the left one). The FB inversion suppresses both phenomena, yielding a more accurate characterization of the ground truth DoI.

Fig. 13 compares the data with 50% noise, noise-free data, and reconstructed data obtained using different methods. In this figure, the four rows from top to bottom correspond to the fields at all the receivers excited by transmitters located at 2.52 km, 7.48 km, 12.52 km and 17.48 km, while the four columns from left to right denote the \log_{10} amplitude for 0.25 Hz data, phase for 0.25 Hz data, \log_{10} amplitude for 0.75 Hz data and phase for 0.75 Hz data. The final DMs for L_2 , WL_2 and FB inversions are 0.0328, 0.0322 and 0.0319, respectively, all close to the noise DM of 0.0322. Rather than fitting the noise-contaminated data, the reconstructed data converge more closely to the clean data, as indicated by the dashed lines in Fig. 13, and data points with strongly deviating noise values are not fitted by any method. This aligns well with our expectation of a sound inversion algorithm that fits

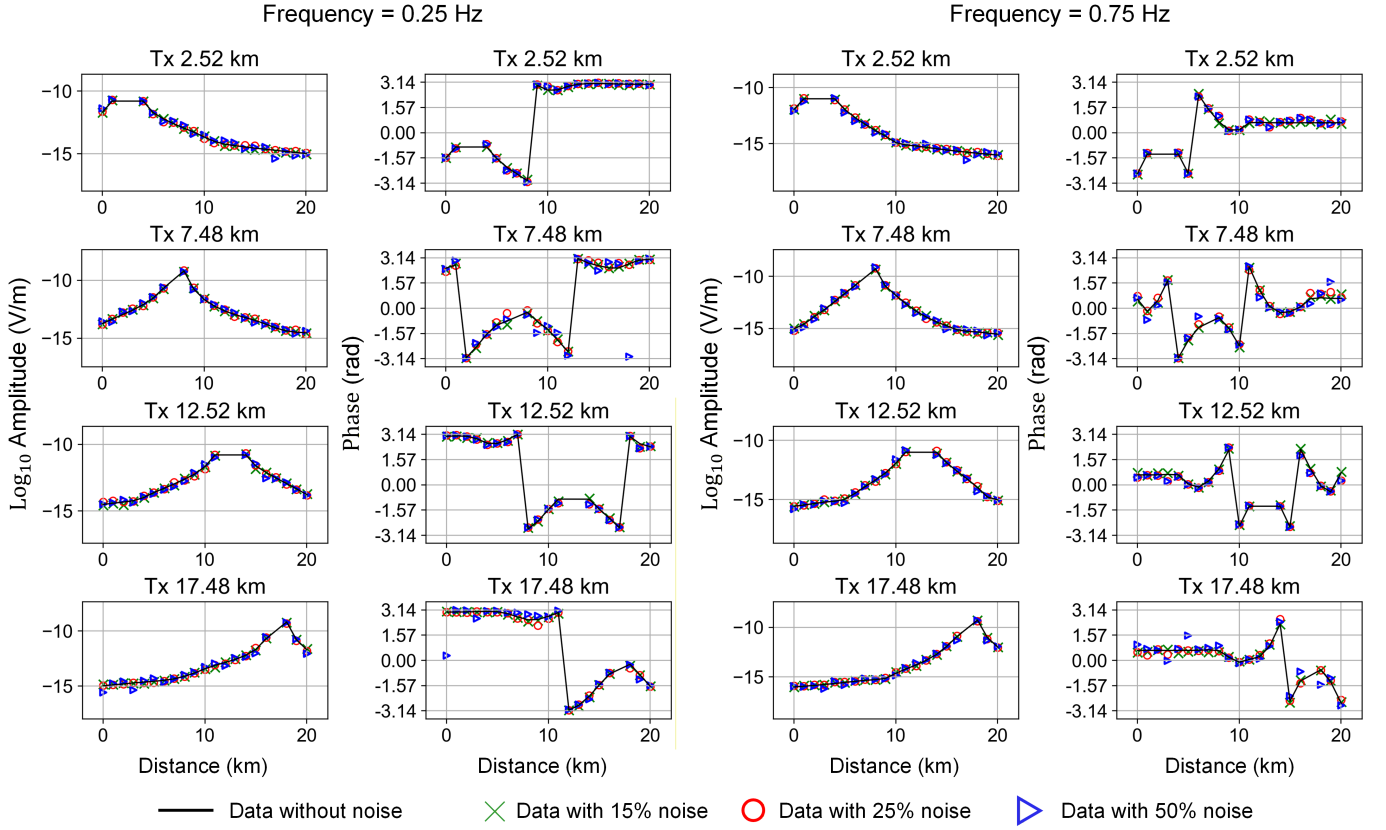


Fig. 10: The comparison between the noise-free simulated data, data with 15% noise, 25% noise and 50% noise, corresponding to test model C. The four columns from left to right respectively show the \log_{10} amplitude of 0.25 Hz data, phase of 0.25 Hz data, \log_{10} amplitude of 0.75 Hz data, and phase of 0.75 Hz data. The four rows from top to bottom show the fields at all active receivers with the transmitter excited at 2.52 km, 7.48 km, 12.52 km, and 17.48 km horizontally.

the overall data trend while excluding extreme anomalous data points.

We note that this experiment further verifies the generalization capability of the proposed deep-learning-assisted FB inversion. Because the neural parameters are decoupled from the forward problem and inference is performed only in the conductivity domain, the trained network can generalize across surveys with different measurement noise distributions, with a low risk of generalization failure.

D. Complex Model Test with Noise

We set up a more complex model (test model D) following [17] (Fig. 13, in *Marine Prospecting Study* section), as shown in Fig. 14. The domain of investigation is 20 km in width and 4.8–5.8 km in depth. The seabed has a varying upper surface, with depths ranging from 1 to 2 km below sea level. The resistivities of the seawater, sedimentary layer, and basement are 0.3, 0.6, and 100 Ωm , respectively. Two resistive blocks are embedded within the sedimentary layer. The thick block has a resistivity of 900 Ωm , is located between depths of 2.6 and 3.4 km, and extends horizontally for 7 km. The thin block has a resistivity of 50 Ωm , is located between depths of 2.1 and 2.4 km, and extends horizontally for 4 km.

The adopted non-uniform mesh contains 251 grids in the horizontal direction and 146 grids in the vertical direction.

Twenty-one receivers and forty-one transmitters are uniformly distributed horizontally, and positioned at the seabed surface and 50 m above the seabed, respectively. The locations of the transmitters and receivers are denoted by red circles and black crosses in Fig. 14, respectively. The operating frequencies are 0.1 and 1 Hz. Gaussian noise with a level of 25% is added to the simulated data, introducing a data misfit of 0.0131.

L_2 , WL_2 and FB inversions are conducted to recover test model D. The initial model is the same for all the three inversions, with the sedimentary resistivity set to a uniform value of 0.6 Ωm . Figs. 15a–15d show the initial model and reconstructions recovered by L_2 , WL_2 and FB inversions, respectively, and Fig. 16 shows the loss function curves of the inversions. For the FB inversion, because irregular DoI cannot be directly processed by the VAE, it is mapped to a regular rectangular region that fully encloses the DoI, and the pixels outside the DoI are filled with representative attribute values within the DoI. In our work, the regular region is set to the entire 20 km by 6.8 km region, as shown in Fig. 14, and the undefined pixels are filled with the resistivity value of the sedimentary background. The *projection steps* are applied at iterations 12, 15 and 18. At the early stage of inversion, the conductivity distribution within the DoI in intermediate models is chaotic and differs from the ground truth; therefore, in our experience, the recovered model in FB inversion usually need

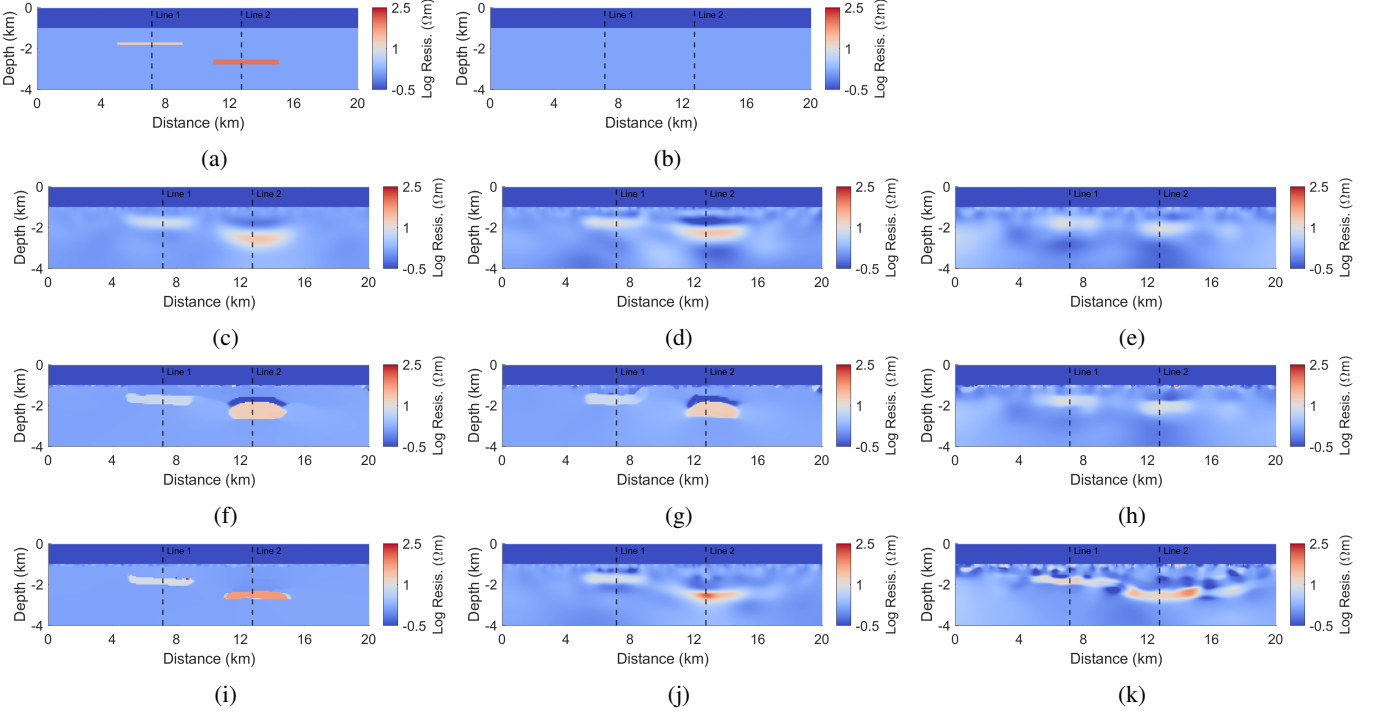


Fig. 11: Fig. 11a: Test model C. Fig. 11b: Initial model for the inversion of test model C data. Figs. 11c–11k: The three rows from top to bottom represent inversions with L_2 regularization, WL_2 regularization and feature-based inversion, and the three columns from left to right show reconstructions corresponding to noise levels of 15%, 25% and 50%.

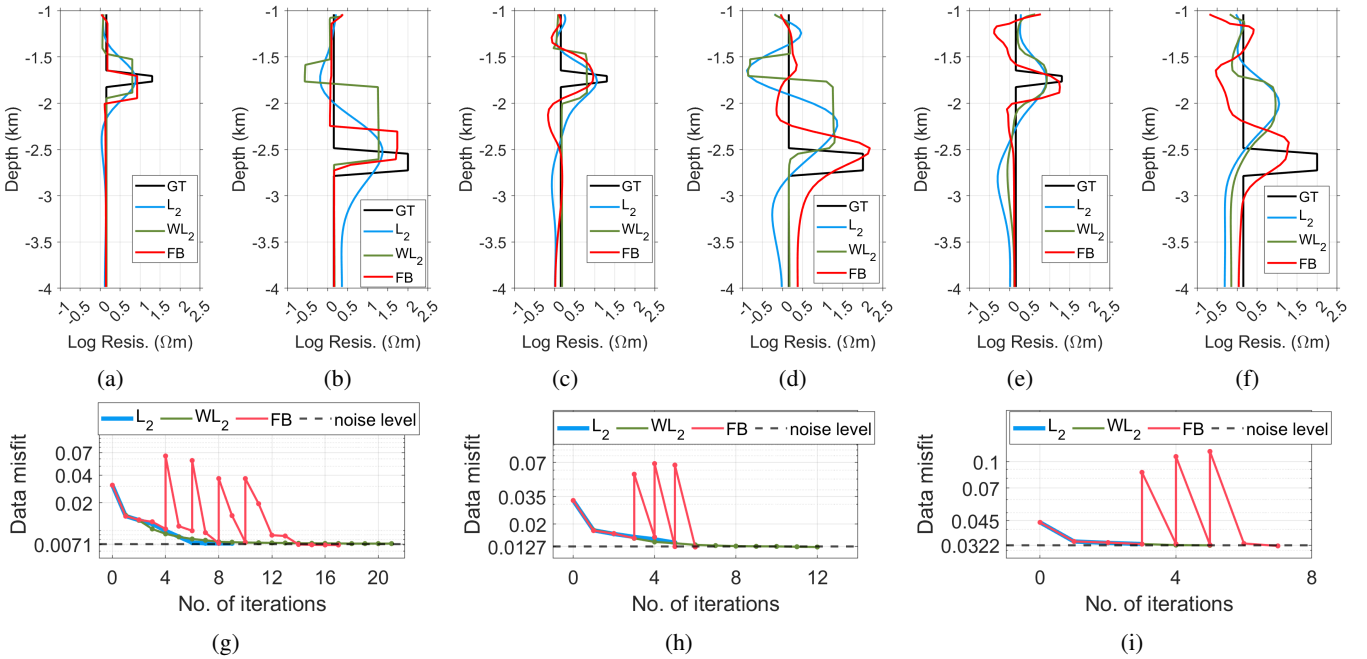


Fig. 12: Figs. 12a and 12b respectively show the ground truth and recovered resistivity curves at Line1 and Line2 (the locations are denoted with black dash lines in Fig. 11a), and Fig. 12g display the data misfit curves in the data inversion of test model C, under 15% noise. Similarly, Figs. 12c, 12d and 12h show the resistivity curves corresponding to Line1 and Line2 in Fig. 11a and data misfit curves under 25% noise. Figs. 12e, 12f and 12i show the resistivity curves corresponding to Line1 and Line2 in Fig. 11a and data misfit curves under 50% noise.

to stabilize first before projection steps are applied. Because test model D has a more complex geometric pattern than

test models A–C, more iterations are required before applying projection steps to allow the recovered model to stabilize.

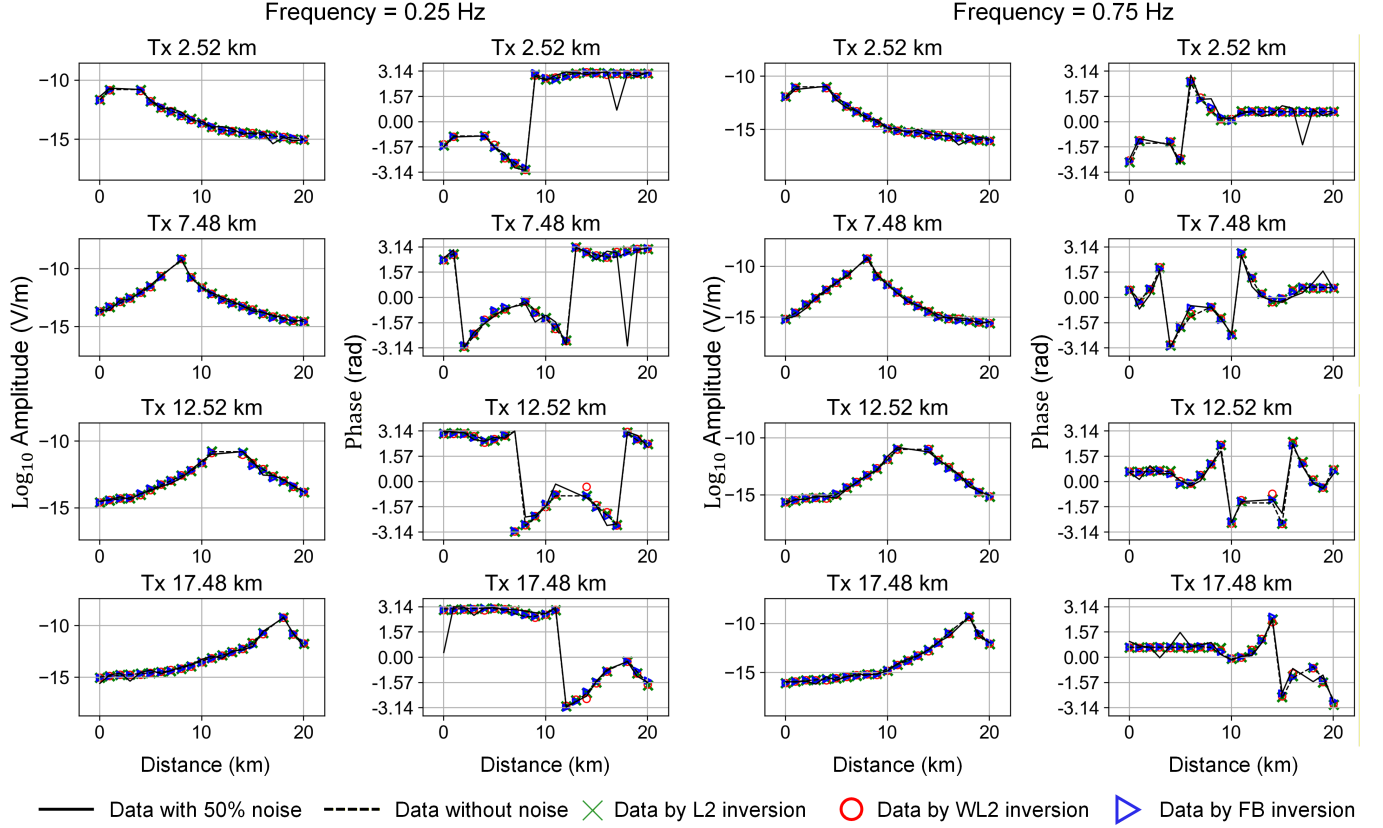


Fig. 13: The comparison between the simulated data with 50% noise, noise-free simulated data, and reconstructed data in L_2 , weighted L_2 and FB inversions, corresponding to test model C. The four columns from left to right respectively show the \log_{10} amplitude of 0.25 Hz data, phase of 0.25 Hz data, \log_{10} amplitude of 0.75 Hz data, and phase of 0.75 Hz data. The four rows from top to bottom show the field measured at all the active receivers with transmitter excited at 2.52 km, 7.48 km, 12.52 km, and 17.48 km horizontally.

All the three inversions converge to similar final DMs, close to the noise level, while FB yields a slightly smaller final DM than two other inversions. The approximated locations of the two anomaly blocks can be identified in all the inversions. Again, consistent with the observations in the previous two sections, the L_2 inversion exhibits blurred boundaries. The right segment of the basement can be observed, but its boundary remains unclear and the recovered resistivity is lower than the true value. In WL_2 inversion, the shapes and boundaries of both blocks are better characterized, but the thickness of the right block is overestimated. In addition, the basement is not properly recovered in the WL_2 inversion. In the FB inversion, the boundaries of both blocks can be clearly identified, and the thickness of the right anomaly is closer to the ground truth than in the L_2 and WL_2 reconstructions, although the left anomaly still appears thinner than its true state. The existence and approximate geometry of the basement are also more clearly characterized than in the L_2 and WL_2 reconstructions, showing a left-lower-right-higher basement topography consistent with test model D. However, the left and right segments show different resistivities: the resistivity of the left segment is reconstructed lower than true value, while the resistivity of the right segment is reconstructed higher than true value. Overall, the FB inversion achieves better imaging

results than the conventional inversions.

The generalization ability is further verified. In this experiment, the subsurface topography is irregular and differs from that in the training dataset and previous experiments, and the model is not included in the training dataset. In addition, the frequencies and spatial distributions of the transmitters and receivers differ from those in previous experiments. However, the FB inversion still produces reasonable results, further demonstrating its generalization capability.

IV. FIELD EXPERIMENT

To further verify the studied inversion, we invert the CSEM data collected in the TrollWest Gas Province (TWGP) in Norway. This is a single-profile survey. Twenty-four EM receivers are distributed on the sea floor. The seawater depth along the line varies from approximately 300 to 360 m, and is commonly approximated as 320 m for modeling. A 230 m long HED transmitter oriented along the survey line direction is towed by a ship and excite EM field with 0.25 Hz continuous square wave signal at different locations, spanning a survey line of over 25 km. In this survey, gas reservoir is buried in Jurassic sandstone, with the maximum thickness about 160 m, a depth about 1400 m and average resistivity around 200-500 Ωm [60]. The conductivity of water bearing Sognefjord Fm.

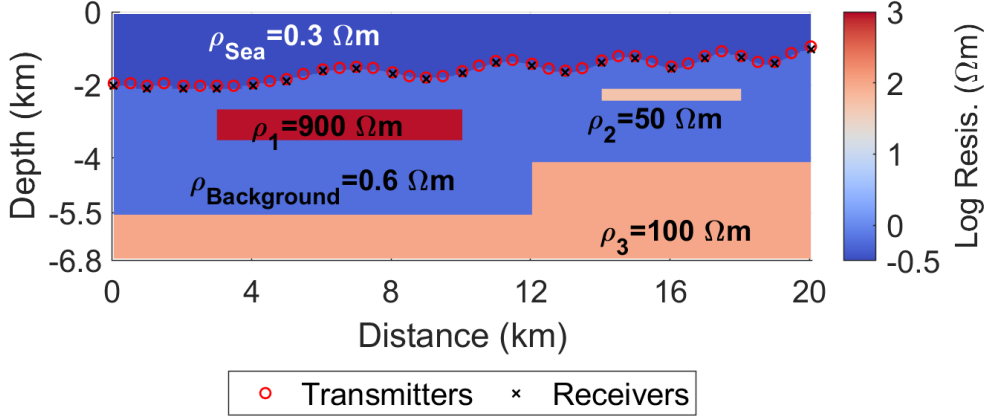


Fig. 14: A visualization of test model D. The seabed has an irregular topography, with twenty-one receivers and forty-one transmitters uniformly distributed horizontally and positioned at the seabed surface and 50 m above the seabed, respectively. The resistivities of the seawater, seabed background, and three resistive layers are labeled in the image.

sands and overburden sediments ranges from 0.5 to 2 S/m. More details about the survey can be found in [60], [61], and for existing inversion work on this survey, please refer to [3], [30].

In the inversion, we use EM data excited at 97 transmitter locations and measured at 23 receivers, as shown in Fig. 17a. Data at 0.25 Hz and 0.75 Hz is reliably extracted. The depth of the sea water is set to 320 m, and the DoI to be reconstructed ranges from 0.32 km to 3.5 km in depth, and from -7 km to 19 km horizontally. The model is discretized into 140 grids vertically and 261 grids horizontally. The mesh used in the inversion is the same with the previous forward modeling. The conductivity of the sea water varies from 4 S/m to 3.3 S/m [3]. Since it's hard to accurately model the excitation strength, we invert the normalized logarithm amplitude (NLA) computed from data d with

$$\text{NLA}_{mnk} = \frac{\log_{10}|d_{mnk}|}{\sum_{m=1}^M \sum_{n=1}^N \log_{10}|d_{mnk}|}, \quad (23)$$

where m, n and k are respectively indices of transmitter, receiver and frequency. We also invert the phase in addition to NLA. At 0.25 Hz, each receiver corresponds to 45 valid data on average, while at 0.75 Hz, each receiver corresponds to 23 valid data on average.

We present L_2 and FB reconstructions. A uniform 0.4 S/m model (see Fig. 17a) is used as the initial model for both the L_2 and FB inversions. The L_2 inversion converges in 14 iterations, with a final DM of 3.38%. Fig. 17b shows the reconstruction obtained from the L_2 inversion. For the FB inversion, the regularization coefficients are the same with L_2 inversion, and the VAE parameters used here is the same with numerical experiments. One *projection step* is configured at iteration 14, and after that the FB inversion takes another 12 steps to converge, resulting a final DM of 2.37%. The projected intermediate model at iteration 14 of FB inversion is shown in Fig. 17c, and the final model by FB inversion is shown in Fig. 17d. The DM curves of both inversions are presented in Fig. 18, and the relative errors between the measured data and

data reconstructed by the two inversions are shown in Fig. 19.

For clarity, we select a vertical trace located at the offset of 7.45 km, and a horizontal trace located at the depth of 1.63 km (denoted by dashed lines in Fig. 17b and 17d), and plot the reconstructions in Fig. 20a and 20b. We can observe that the overall conductivity pattern of TWGP can be recovered by the conventional inversion, that is, the resistive layer buried in the conductive background, with the location and size basically consistent with the prior knowledge. From the L_2 inversion results, the reservoir is interpreted to be located at a depth of approximately 1400–1600 m, with a maximum thickness of about 210 m and a typical thickness of around 100 m. The lateral extent is estimated to be approximately 7.4 km, and the maximum resistivity reaches about 63 Ωm. However, because the overall resistivity contrast is relatively weak, the reservoir boundaries are not sharply resolved. As a result, the estimates of reservoir length and thickness remain ambiguous and show noticeable deviations from prior geological expectations, where the average resistivity is known to be around 200–500 Ωm and the maximum thickness about 160 m [3], [60]. Compared to conventional reconstructions, the features of the resistive layer are clearer in the projected model. From FB reconstruction, we can find that the depth of the reservoir is about 1400 to 1600 meters, with the maximum thickness about 160 m, a typical thickness about 100 m, length about 8 km and the maximum resistivity about 200 Ωm. The reservoir thickness and burial depth recovered by the feature-based inversion show improved agreement with available geological information [60]. In addition, the estimated reservoir length is closer to previously reported inversion results [30], although the maximum recovered resistivity remains slightly lower than the expected values inferred from prior knowledge.

We conclude that the FB inversion achieves improved inversion results compared to conventional inversions; however, in this field inversion case, the improvement is not very pronounced, likely because the conventional inversion already provides reasonably good results. We will investigate

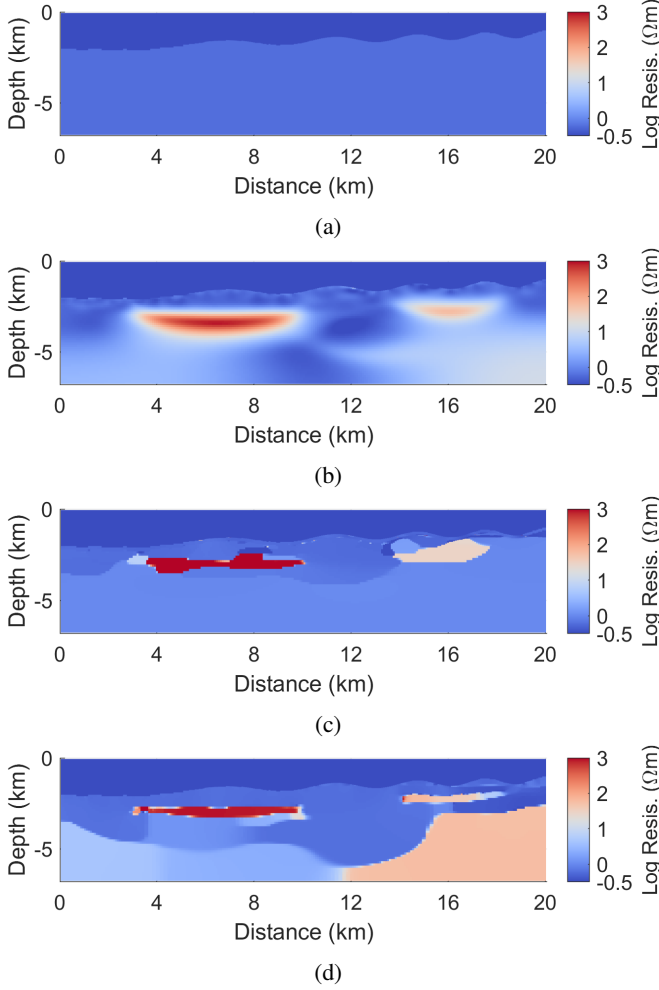


Fig. 15: Fig. 15a: The initial model in the inversions of test model D. Fig. 15b: Model reconstructed by L_2 inversion. Fig. 15c: Model reconstructed by WL_2 inversion. Fig. 15d: Model reconstructed by feature-based inversion.

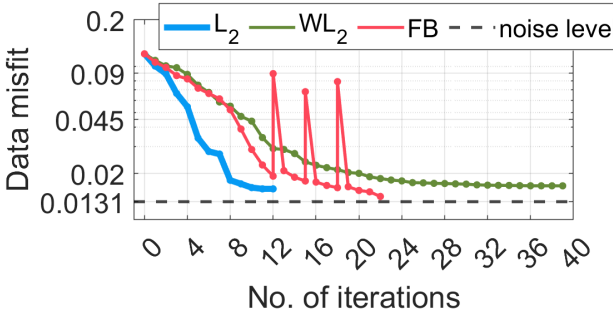


Fig. 16: Data misfit curves of the test model D inversions.

more representative inversion cases to better demonstrate the advantages of the feature-based inversion.

V. CONCLUSION

In this work, we study the feature-based 2.5D marine controlled source electromagnetic (mCSEM) inversion using generative priors. Two-point-five dimensional modeling using

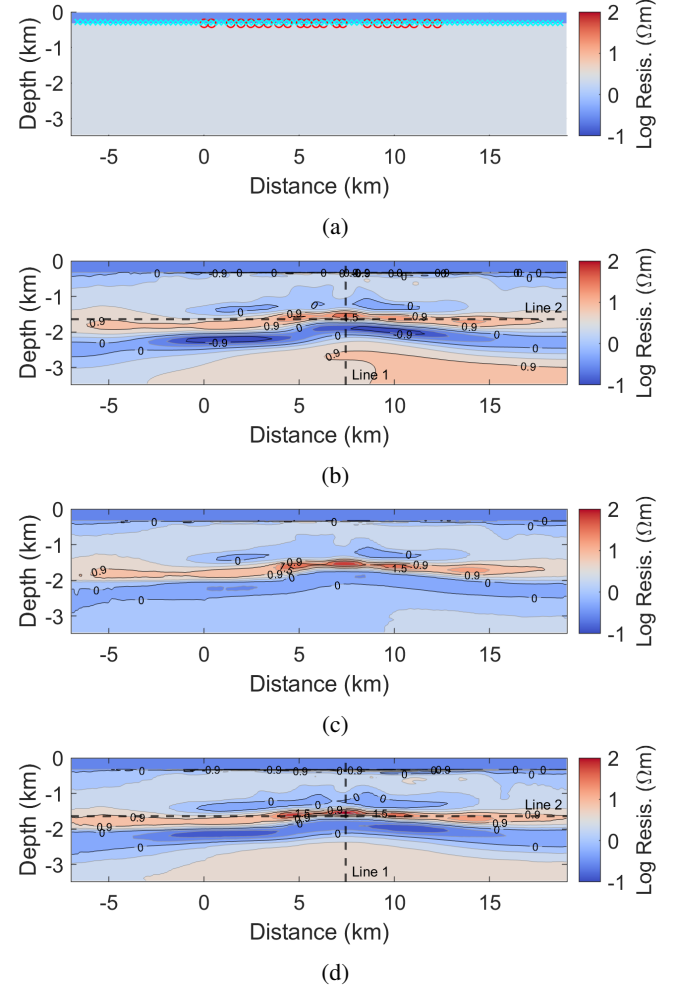


Fig. 17: Fig. 17a: The initial model in the inversions of Troll field data. Fig. 17b: Model reconstructed by L_2 reconstruction. Fig. 17c: Model projected to the VAE output range in FB inversion at iteration 14. Fig. 17d: Model reconstructed by feature-based inversion.

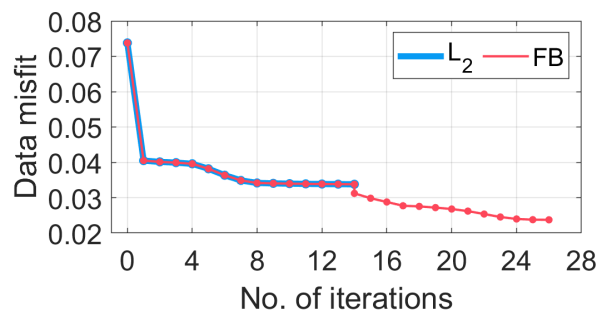


Fig. 18: Data misfit curves of the Troll field data inversions.

finite difference method (FDM) is adopted to compute the response of horizontal electric dipole (HED) excitation in the 2D survey. Generative prior is incorporated in the inversion by reparametrizing the model with the variational autoencoder (VAE). In the inversion, the model is consecutively updated with Gauss-Newton method and projected to the range of the

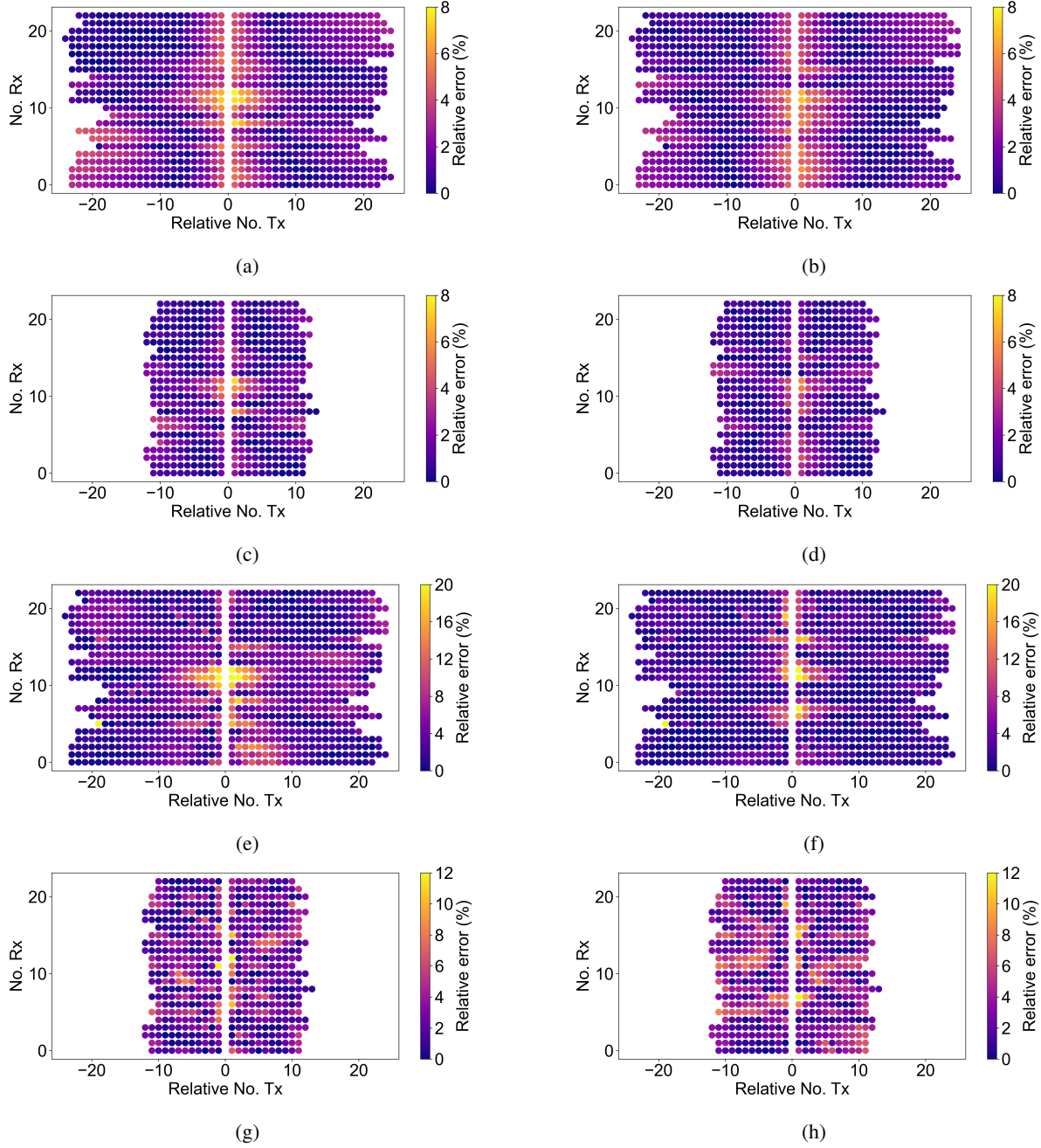


Fig. 19: Visualization of the relative errors between the reconstructed data and measured data, for both normalized logarithm amplitude (NLA) and phase. The four rows respectively represent the NLA relative errors for 0.25 Hz, NLA relative errors for 0.75 Hz, phase relative errors for 0.25 Hz, and phase relative errors for 0.75 Hz. In the first column, the reconstructed data is recovered by L_2 inversion and in the second column, the reconstructed data is recovered by feature-based inversion.

VAE decoder. Both numerical and field experiments verify that the proposed inversion is able to effectively incorporate *a priori* knowledge and improve the reconstruction accuracy and possesses good generalization ability. Future improvements to this work may involve developing more efficient and robust optimization algorithms to eliminate the reliance on heuristics in setting the projection step, as well as optimizing the architecture and training of the VAE, and extending the proposed method to land CSEM inversion.

APPENDIX

METRICS TO EVALUATE INVERSION RESULTS

We introduce some metrics to measure the inversion quality, including data misfit (DM), intersection over union (IoU), mean square error (MSE) and structural similarity (SSIM) [62], as listed in (A1)-(A4):

$$DM = \frac{\|\mathbf{d}_{\text{obs}} - \mathbf{d}_{\text{rec}}\|_2}{\|\mathbf{d}_{\text{obs}}\|_2}, \quad (\text{A1})$$

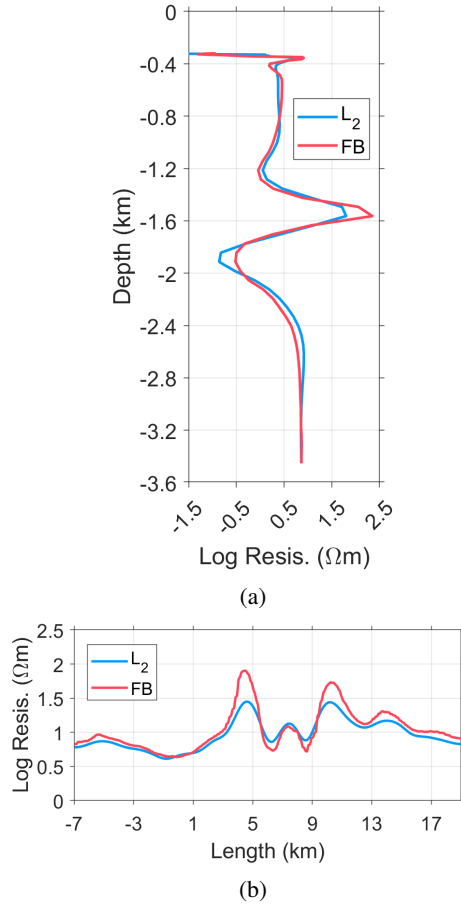


Fig. 20: Fig. 20a: the vertical traces denoted by Line1. Fig. 20b: the horizontal traces denoted by Line2.

and

$$\text{IoU}(\mathbf{I}_{\text{rec}}, \mathbf{I}_{\text{gnd}}) = \frac{|\mathbf{I}_{\text{rec}} \cap \mathbf{I}_{\text{gnd}}|}{|\mathbf{I}_{\text{rec}} \cup \mathbf{I}_{\text{gnd}}|}, \quad (\text{A2})$$

$$\text{MSE} = \|\mathbf{m}_{\text{gnd}} - \mathbf{m}_{\text{rec}}\|_2^2, \quad (\text{A3})$$

$$\text{SSIM} = \frac{(2\mu_x\mu_y + C_1)(2\sigma_{xy} + C_2)}{(\mu_x^2 + \mu_y^2 + C_1)(\sigma_x^2 + \sigma_y^2 + C_2)}. \quad (\text{A4})$$

Here, \mathbf{d}_{obs} and \mathbf{d}_{rec} are observed and reconstructed data. \mathbf{I}_{gnd} is the 0-1 identification function, in which 1 pixels indicate the target reservoir and 0 pixels indicate the background in the ground truth model. \mathbf{I}_{rec} is also a 0-1 identification function, in which 1 pixels indicate where the value of the reconstructed conductivity is greater than half the peak value. \mathbf{m}_{gnd} and \mathbf{m}_{rec} are respectively the ground truth and reconstructed model. $\mu_x, \mu_y, \sigma_x, \sigma_y$ and σ_{xy} denote the mean, standard deviation and covariance between two images x and y , and C_1 and C_2 are two positive constants.

ACKNOWLEDGMENTS

HZ would like to express his gratitude to Prof. Yoram Bresler from the University of Illinois at Urbana-Champaign for fruitful discussions on generative-prior-regularized inverse problems.

REFERENCES

- [1] S. Constable, "Marine electromagnetic methods—A new tool for offshore exploration," *The Leading Edge*, vol. 25, no. 4, pp. 438–444, 2006.
- [2] A. Gribenko and M. Zhdanov, "Rigorous 3D inversion of marine CSEM data based on the integral equation method," *Geophysics*, vol. 72, no. 2, pp. WA73–WA84, 2007.
- [3] A. Abubakar, T. Habashy, V. Druskin, L. Knizhnerman, and D. Alumbaugh, "2.5 D forward and inverse modeling for interpreting low-frequency electromagnetic measurements," *Geophysics*, vol. 73, no. 4, pp. F165–F177, 2008.
- [4] M. Commer and G. A. Newman, "New advances in three-dimensional controlled-source electromagnetic inversion," *Geophysical Journal International*, vol. 172, no. 2, pp. 513–535, 2008.
- [5] K. Key, "1D inversion of multicomponent, multifrequency marine CSEM data: Methodology and synthetic studies for resolving thin resistive layers," *Geophysics*, vol. 74, no. 2, pp. F9–F20, 2009.
- [6] Y. Li and S. Dai, "Finite element modelling of marine controlled-source electromagnetic responses in two-dimensional dipping anisotropic conductivity structures," *Geophysical Journal International*, vol. 185, no. 2, pp. 622–636, 05 2011.
- [7] K. Key and J. Oval, "A parallel goal-oriented adaptive finite element method for 2.5-D electromagnetic modelling," *Geophysical Journal International*, vol. 186, no. 1, pp. 137–154, 07 2011.
- [8] V. Brown, M. Hoversten, K. Key, and J. Chen, "Resolution of reservoir scale electrical anisotropy from marine CSEM data," *Geophysics*, vol. 77, no. 2, pp. E147–E158, 2012.
- [9] S. Kang, K. Noh, S. J. Seol, and J. Byun, "mCSEM inversion for CO₂ sequestration monitoring at a deep brine aquifer in a shallow sea," *Exploration Geophysics*, vol. 46, no. 3, pp. 236–252, 2015.
- [10] K. Key, "MARE2DEM: a 2-D inversion code for controlled-source electromagnetic and magnetotelluric data," *Geophysical Journal International*, vol. 207, no. 1, pp. 571–588, 2016.
- [11] Y. Zhou, M. Zhuang, L. Shi, G. Cai, N. Liu, and Q. H. Liu, "Spectral-element method with divergence-free constrain for 2.5-D marine CSEM hydrocarbon exploration," *IEEE Geoscience and Remote Sensing Letters*, vol. 14, no. 11, pp. 1973–1977, 2017.
- [12] S. Oh, K. Noh, S. J. Seol, and J. Byun, "Cooperative deep learning inversion of controlled-source electromagnetic data for salt delineation," *Geophysics*, vol. 85, no. 4, pp. E121–E137, 2020.
- [13] O. Ohwoghere-Asuma, I. F. Chinyem, K. E. Aweto, and R. Iserhien-Emekeme, "The use of very low-frequency electromagnetic survey in the mapping of groundwater condition in oporoza-gbamaratu area of the Niger Delta," *Applied Water Science*, vol. 10, no. 7, p. 164, Jun. 2020. [Online]. Available: <https://doi.org/10.1007/s13201-020-01244-w>
- [14] J. Li, Y. Li, Y. Liu, K. Spitzer, and B. Han, "3-D marine CSEM forward modeling with general anisotropy using an adaptive finite-element method," *IEEE Geoscience and Remote Sensing Letters*, vol. 18, no. 11, pp. 1936–1940, 2021.
- [15] B. Wu, Y. Liao, H. Chen, L. Chen, S. Ren, S. Xiao, Y. Yang, Y. Yang, and H. Peng, "Fine Detection and Analysis of Hidden Karst in Wellsite with Quasi-Three-Dimensional TDEM Based on Lateral Constraint," *Geofluids*, vol. 2023, no. 1, p. 2766524, 2023, _eprint: <https://onlinelibrary.wiley.com/doi/pdf/10.1155/2023/2766524>. [Online]. Available: <https://onlinelibrary.wiley.com/doi/abs/10.1155/2023/2766524>
- [16] M. Farzamian, F. Bouksila, A. M. Paz, F. M. Santos, N. Zemni, F. Slama, A. Ben Slimane, T. Selim, and J. Triantafilis, "Landscape-scale mapping of soil salinity with multi-height electromagnetic induction and quasi-3d inversion in Saharan Oasis, Tunisia," *Agricultural Water Management*, vol. 284, p. 108330, Jun. 2023. [Online]. Available: <https://www.sciencedirect.com/science/article/pii/S0378377423001956>
- [17] C. Qin, W. He, X. Wang, and N. Zhao, "3-D joint inversion of MT and CSEM data based on adaptive finite element forward modeling," *IEEE Transactions on Geoscience and Remote Sensing*, 2024.
- [18] H. Liang, R. Gao, C. Yin, Y. Su, Z. He, and Y. Liu, "Physics-driven deep-learning for marine CSEM data inversion," *Journal of Applied Geophysics*, vol. 229, p. 105474, 2024.
- [19] Y. Lu, H. Tan, D. Yang, Z. Wang, Y. Yang, L. Yan, W. Wan, and H. Wang, "A Feasibility Study of Land CSEM Surveys With a Near-Casing Source for Hydraulic Fracturing Monitoring," *IEEE Access*, vol. 12, pp. 32 238–32 252, 2024. [Online]. Available: <https://ieeexplore.ieee.org/document/10445415>
- [20] W. Gao, X. Wang, Z. Hui, and L. Mao, "Two-Dimensional imaging for 3D ground frequency domain CSEM based on vector finite element," *IEEE Transactions on Geoscience and Remote Sensing*, 2025.

- [21] A. N. Tikhonov, "Regularization of incorrectly posed problems." *Soviet Mathematics Doklady*, 1963.
- [22] M. Benning and M. Burger, "Modern regularization methods for inverse problems," *Acta Numerica*, vol. 27, pp. 1–111, 2018.
- [23] Y. Liu, X. Ma, L. Wang, C. Yin, X. Ren, B. Zhang, and Y. Su, "A robust approach for geo-electromagnetic sounding data inversion using l_1 -norm misfit and adaptive moment estimation," *IEEE Transactions on Geoscience and Remote Sensing*, 2024.
- [24] A. Marcuello-Pascual, P. Kaikonen, and J. Pous, "2-D inversion of MT data with a variable model geometry," *Geophysical Journal International*, vol. 110, no. 2, pp. 297–304, 08 1992.
- [25] E. Auken and A. V. Christiansen, "Layered and laterally constrained 2D inversion of resistivity data," *Geophysics*, vol. 69, no. 3, pp. 752–761, 2004.
- [26] M. Li, A. Abubakar, T. M. Habashy, and Y. Zhang, "Inversion of controlled-source electromagnetic data using a model-based approach," *Geophysical Prospecting*, vol. 58, no. 3, pp. 455–467, 2010.
- [27] J. Chen, G. M. Hoversten, K. Key, G. Nordquist, and W. Cumming, "Stochastic inversion of magnetotelluric data using a sharp boundary parameterization and application to a geothermal site," *Geophysics*, vol. 77, no. 4, pp. E265–E279, 2012.
- [28] C. G. Nittinger and M. Becken, "Inversion of magnetotelluric data in a sparse model domain," *Geophysical Journal International*, vol. 206, no. 2, pp. 1398–1409, 2016.
- [29] Y. Liu, C. G. Farquharson, C. Yin, and V. C. Baranwal, "Wavelet-based 3-D inversion for frequency-domain airborne EM data," *Geophysical Journal International*, vol. 213, no. 1, pp. 1–15, 2018.
- [30] A. Abubakar, T. Habashy, Y. Lin, and M. Li, "A model-compression scheme for nonlinear electromagnetic inversions," *Geophysics*, vol. 77, no. 5, pp. E379–E389, 2012.
- [31] T. Lochbühler, S. J. Breen, R. L. Detwiler, J. A. Vrugt, and N. Linde, "Probabilistic electrical resistivity tomography of a CO₂ sequestration analog," *Journal of Applied Geophysics*, vol. 107, pp. 80–92, 2014.
- [32] L.-Y. Chiao and B.-Y. Kuo, "Multiscale seismic tomography," *Geophysical Journal International*, vol. 145, no. 2, pp. 517–527, 2001.
- [33] L.-Y. Chiao and W.-T. Liang, "Multiresolution parameterization for geophysical inverse problems," *Geophysics*, vol. 68, no. 1, pp. 199–209, 2003.
- [34] I. Loris, G. Nolet, I. Daubechies, and F. Dahlen, "Tomographic inversion using l_1 -norm regularization of wavelet coefficients," *Geophysical Journal International*, vol. 170, no. 1, pp. 359–370, 2007.
- [35] S.-H. Hung, W.-P. Chen, L.-Y. Chiao, and T.-L. Tseng, "First multi-scale, finite-frequency tomography illuminates 3-D anatomy of the Tibetan plateau," *Geophysical Research Letters*, vol. 37, no. 6, 2010.
- [36] E. K. Oware, J. Irving, and T. Hermans, "Basis-constrained Bayesian Markov-chain Monte Carlo difference inversion for geoelectrical monitoring of hydrogeologic processes," *Geophysics*, vol. 84, no. 4, pp. A37–A42, 2019.
- [37] Z. Zhao, J. C. Ye, and Y. Bresler, "Generative models for inverse imaging problems: From mathematical foundations to physics-driven applications," *IEEE Signal Processing Magazine*, vol. 40, no. 1, pp. 148–163, 2023.
- [38] Y. Song, L. Shen, L. Xing, and S. Ermon, "Solving inverse problems in medical imaging with score-based generative models," *arXiv preprint arXiv:2111.08005*, 2021.
- [39] H. Chung, D. Ryu, M. T. McCann, M. L. Klasky, and J. C. Ye, "Solving 3D inverse problems using pre-trained 2D diffusion models," in *Proceedings of the IEEE/CVF Conference on Computer Vision and Pattern Recognition*, 2023, pp. 22 542–22 551.
- [40] R. Guo, Z. Lin, M. Li, F. Yang, S. Xu, and A. Abubakar, "A non-linear model compression scheme based on variational autoencoder for microwave data inversion," *IEEE Transactions on Antennas and Propagation*, vol. 70, no. 11, pp. 11 059–11 069, 2022.
- [41] R. Guo, Z. Lin, J. Xin, M. Li, F. Yang, S. Xu, and A. Abubakar, "Three dimensional microwave data inversion in feature space for stroke imaging," *IEEE Transactions on Medical Imaging*, vol. 43, no. 4, pp. 1365–1376, 2023.
- [42] M. Asim, F. Shamshad, and A. Ahmed, "Blind image deconvolution using deep generative priors," *IEEE Transactions on Computational Imaging*, vol. 6, pp. 1493–1506, 2020.
- [43] L. Rout, N. Raoof, G. Daras, C. Caramanis, A. Dimakis, and S. Shakkottai, "Solving linear inverse problems provably via posterior sampling with latent diffusion models," *Advances in Neural Information Processing Systems*, vol. 36, pp. 49 960–49 990, 2023.
- [44] Z. Wang, S. Wang, C. Zhou, and W. Cheng, "Dual Wasserstein generative adversarial network condition: A generative adversarial network-based acoustic impedance inversion method," *Geophysics*, vol. 87, no. 6, pp. R401–R411, 2022.
- [45] H. Zhou, R. Guo, M. Li, F. Yang, S. Xu, and A. Abubakar, "Feature-based magnetotelluric inversion by variational autoencoder using a subdomain encoding scheme," *Geophysics*, vol. 89, no. 1, pp. WA67–WA83, 2024.
- [46] A. Bora, A. Jalal, E. Price, and A. G. Dimakis, "Compressed sensing using generative models," in *International conference on machine learning*. PMLR, 2017, pp. 537–546.
- [47] V. Shah and C. Hegde, "Solving linear inverse problems using gan priors: An algorithm with provable guarantees," in *2018 IEEE international conference on acoustics, speech and signal processing (ICASSP)*. IEEE, 2018, pp. 4609–4613.
- [48] A. Raj, Y. Li, and Y. Bresler, "GAN-based projector for faster recovery with convergence guarantees in linear inverse problems," in *Proceedings of the IEEE/CVF international conference on computer vision*, 2019, pp. 5602–5611.
- [49] Q. Li and Y. Luo, "Using GAN priors for ultrahigh resolution seismic inversion," in *Seg international exposition and annual meeting*. SEG, 2019, p. D023S015R004.
- [50] M. N. Nabighian, *Electromagnetic methods in applied geophysics: Volume 1, theory*. Society of Exploration Geophysicists, 1988.
- [51] P. McGillivray, D. Oldenburg, R. Ellis, and T. Habashy, "Calculation of sensitivities for the frequency-domain electromagnetic problem," *Geophysical Journal International*, vol. 116, no. 1, pp. 1–4, 1994.
- [52] D. P. Kingma and M. Welling, "Auto-encoding variational bayes," *arXiv preprint arXiv:1312.6114*, 2013.
- [53] —, "An introduction to variational autoencoders," *Foundations and Trends® in Machine Learning*, vol. 12, no. 4, pp. 307–392, 2019.
- [54] R. Rombach, A. Blattmann, D. Lorenz, P. Esser, and B. Ommer, "High-resolution image synthesis with latent diffusion models," in *Proceedings of the IEEE/CVF conference on computer vision and pattern recognition*, 2022, pp. 10 684–10 695.
- [55] A. Krizhevsky, I. Sutskever, and G. E. Hinton, "Imagenet classification with deep convolutional neural networks," *Advances in neural information processing systems*, vol. 25, 2012.
- [56] T. Habashy and A. Abubakar, "A general framework for constraint minimization for the inversion of electromagnetic measurements," *Progress in electromagnetics Research*, vol. 46, pp. 265–312, 2004.
- [57] M. L. Gonçalves and T. C. Menezes, "Gauss-Newton methods with approximate projections for solving constrained nonlinear least squares problems," *Journal of Complexity*, vol. 58, p. 101459, 2020.
- [58] Y. Nabou, L. Toma, and I. Necoara, "Modified projected Gauss-Newton method for constrained nonlinear least-squares: application to power flow analysis," in *2023 European Control Conference (ECC)*. IEEE, 2023, pp. 1–6.
- [59] D. P. Kingma and J. Ba, "Adam: A method for stochastic optimization," 2017.
- [60] S. Johansen, H. Amundsen, T. Røsten, S. Ellingsrud, T. Eidesmo, and A. Bhuiyan, "Subsurface hydrocarbons detected by electromagnetic sounding," *First break*, vol. 23, no. 3, 2005.
- [61] G. M. Hoversten, T. Røsten, K. Hokstad, D. Alumbaugh, S. Horne, and G. A. Newman, "Integration of multiple electromagnetic imaging and inversion techniques for prospect evaluation," in *SEG Technical Program Expanded Abstracts 2006*. Society of Exploration Geophysicists, 2006, pp. 719–723.
- [62] Z. Wang, A. C. Bovik, H. R. Sheikh, and E. P. Simoncelli, "Image quality assessment: from error visibility to structural similarity," *IEEE transactions on image processing*, vol. 13, no. 4, pp. 600–612, 2004.